



A single-ion focused 393nm laser for photon generation and qubit control

A master's thesis submitted to the faculty of mathematics, computer science
and physics, of the University of Innsbruck
in partial fulfillment of the requirements for the degree of

Master of Science (MSc)

carried out at the Institute of Experimental Physics under the supervision of
o.Univ.-Prof. Dr. Rainer Blatt,
Dr. Ben Lanyon

Presented by

Marco Canteri

Abstract

boh

Contents

1	Introduction	1
2	Theoretical framework	5
2.1	Quantum logic with trapped ions	5
2.1.1	Quantum computer and quantum gates	5
2.1.2	Ion qubits and laser-ion interactions	7
2.1.2.1	Three-level model	11
2.1.2.2	Dissipative processes	12
2.2	Quantum networking with trapped ions	12
2.2.1	General introduction	12
2.2.2	Cavity QED	13
2.2.3	Photon generation	14
2.3	Basics of ion trapping	16
2.3.1	Linear Paul trap	16
2.3.2	Ion strings	18
2.3.3	Doppler cooling and detection	19
2.4	Laser beam	21
2.4.1	Gaussian beams	21
2.4.2	Beam steering via AOD's	24
2.5	Experiments model	26
2.5.1	Addressed photon generation	26
2.5.2	Addressed qubit manipulation	26
3	Existing experimental system	29
3.1	Ion trap and key techniques	29
3.1.1	Calcium Ions	29
3.1.2	Trapping, cooling, and state readout	30
3.2	393 nm laser	32
3.3	Experiment control	33
4	Design and simulation of the addressing setup	37
4.1	Addressing system overview and requirements	37
4.2	Objective and AOD	39
4.3	Design simulation	40
4.4	Physical implementation	43
5	Experimental results	47
5.1	AOD	47

5.2	Full test setup characterization	48
5.2.1	Waist: Knife-Edge method	49
5.2.2	Waist: Camera	50
5.2.3	Polarization	52
5.2.4	Stability	53
5.3	Final installed system	56
5.3.1	Ramsey interferometry	56
5.3.2	Photon production	58
5.4	Final properties summary	60
6	Conclusions and outlook	61
	References	63

Chapter 1

Introduction

The next natural step in technology advancement is represented by quantum technology, as it offers a radically new approach for computation, communication, simulation, and metrology [1]. All of these fields can greatly flourish with the development of quantum computers and quantum networks. Classical computers are limited in solving some particular problems that scale exponentially, and therefore a new approach is needed. Quantum computing can exploit particular features of quantum mechanics that have no classical counterparts, this allows for a speed up for a certain class of problems such as factorizing numbers [2], or searching in a database [3]. Moreover, simulating nature at its quantum level is a hard task for classical computer, while quantum computers are naturally prone to simulate quantum dynamics.

Quantum networks also bring new additional features, and several benefits to communication. The concept of a quantum internet is to have a quantum channel along side with the classical channel, enabling the transmission of quantum information [4]. The task of building a quantum network is not trivial, as there are fundamental differences with a classical link. Although the medium can be the same, such as optical fiber, a quantum network must have additional abilities, such as distributing entanglement, or transmitting quantum states. However, once achieved, quantum networks have several applications: cryptographic wise they allow for more secure information transmission through Quantum Key Distribution [5], secure identification [6], blind quantum computation [7] and more [4]. Outside cryptography, quantum networks finds applications in metrology: entanglement can be exploited to improve clock synchronization [8], and extend telescope's baseline [9]. Furthermore, quantum networks offer more efficient solutions to distributed system problems [10].

A set of criteria exists to assess the viability of a realistic implementation of quantum computers and quantum networks [11], several platforms have been proposed and implemented trying to satisfy these criteria. Ion trapping has already fulfilled all criteria experimentally [12] and it shows great potential for a possible large scale quantum computer. The idea is simple, qubits are encoded in the electronic state of single trapped ion in a Paul trap. Manipulation can be done with laser pulses [13] and by placing a cavity, an ion trap gains network abilities [14].

However, still a lot of challenges needs to be addressed for a quantum computer to outperform a classical one. Due to the incredible delicate nature of qubits, they are subject to decoherence which harms the successfulness and computational power of quantum computers. Therefore, scaling the number of qubit has been proven to be a

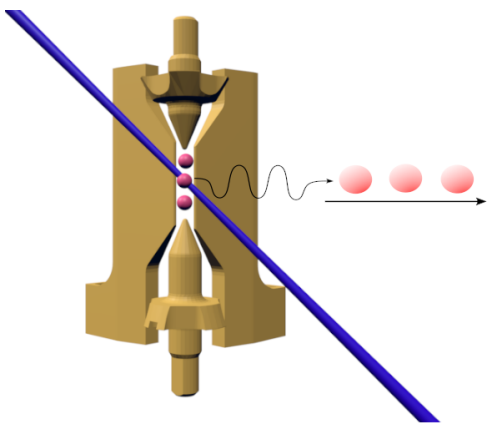
difficult engineeristic challenge. Several solutions are possible: the number of qubits can scale; the dimension of qubits can decrease; or qubits can be linked together. The last solution is the approach at the base of quantum networks. The idea is to link several quantum computers to create a cluster of nodes that can work jointly.

It is in this context that this thesis arises. Currently there is an ongoing project of building a three node quantum network between two buildings on the campus of the University of Innsbruck. The third node is located in IQOQI, where the thesis took place. Here an ion trap is used as node of the network and it is connected to the other traps via a 400m fiber link. A 393nm lasers is responsible for the generation of the transmitted photons via a cavity enhanced Raman process [14]. At the time of this thesis' start, the 393nm laser was shining on every ion in the trap. In this case, if an ion string were to be loaded, the light would couple to every ions and there would be no control over the single ion-photon pair. An addressing setup enables the generation of single photons from individual ions which opens up several possibilities in computer-network interfacing: multi-ion-multi-photon states can be generated, a quantum node gains quantum memory capabilities, and the possibility of multiplexing increases drastically the network bandwidth.

To overcome this limitation, an optical setup for the 393nm laser had to be built with the purpose of focusing the light to a single ion in a string. Moreover the setup should have the ability to steer the beam on a fast scale $\sim \mu\text{s}$ and focus it on a different ion. The goal of this thesis was to design and build such a system. The setup is per se not complex, but the design is critical, ions separation is typical in the order of μm , which means the light should be focused down to $1 - 2 \mu\text{m}$, at the limits of the optical elements involved. The steering part is achieved with an acousto-optical deflector (AOD), such device deflects the laser light on microsecond timescales proportionally to the applied input frequency allowing to control remotely the beam pointing of the system.

Once completed, the system will allow to manipulate single ions in a string in two different ways differentiated by the laser regime. Hence, the final goal of the thesis is to perform two experiments that demonstrate the functionalities of the system:

SINGLE ION PHOTON GENERATION



The first experiment is photon generation, a single laser pulse can trigger the generation of a single photon in a cavity via a Raman process [14]. The process requires the addressed ion to be coupled to the cavity electric field, both the cavity and the laser pulse must be correctly detuned to suppress spontaneous scattering and maximize the probability of photon production. With the AOD the laser pulse is steered and aimed at different ions in μs time, thus enabling the creation of photon trains. This enriches the capabilities of the interface between the ion quantum computer and the photonic network channel, as outlined above.

SINGLE ION QUBIT MANIPULATION

The second experiment is qubit manipulation. A phase gate [15] over a single qubit is implemented. In the off resonant regime, the laser induces AC Stark shift on the $|0\rangle$ state

of the qubit, shifting the relative phase of the qubit state. In order to measure the AC Stark shift we want to perform Ramsey interferometry [16], where between the two $\pi/2$ pulses a detuned Stark pulse is introduced. This pulse shift the relative phase of the qubit and therefore the amount of Stark shift can be inferred from the final qubit state. The gate is part of the universal set of quantum gates [15], and it is therefore a building block of a full implementation of a quantum computer.

This work is presented in the following way: Chapter 2 is devoted to the theoretical background necessary to understand the rest of the work. Here the foundations of quantum computing and networking are laid down, along with the basic concepts of ion trapping, and Gaussian beams; Chapter 3 presents the existing experimental setup, i.e. the already built and working blocks of the experiment where the setup designed in this thesis has been added; Chapter 4 is the core of the thesis, here the final design made with the software Zemax and simulations of different aspects of the project are introduced and presented; Chapter 5 contains all the experimental results obtained. It is divided in two parts: First, the setup was built on a spare optical table, here we had the freedom to test different key properties of the performance of the system and decide whether or not it was satisfactory. After having the certainty that the system will work, the setup was transferred and aligned on the main experiment where limited access did not allow for easy performance testing. Here, different and more advanced experimental quantum optics methods had to be used to check if the system was working properly. The description and discussion of these results are in the second part of chapter 5. Lastly, in chapter 6 a conclusion with a summary and a future outlook is given.



Chapter 2

Theoretical framework

Quantum computing is based on a general framework that does not depend on the physical platform. Here, important concepts such as qubit, and quantum operations are described from a theoretical point of view, before showing how we can realize them with trapped ions. The same goes with quantum networking, the concept and the realization can be treated separately and they will be described in this chapter. Furthermore, in this chapter we will take a look into Gaussian beams and their properties. Since that is the shape emitted by laser, it is important to understand their characteristic and how to manipulate them. Lastly, Acousto-optical interactions are introduced and studied to give an idea of how AODs work and how they can be used to steer a laser beam.

2.1 Quantum logic with trapped ions

2.1.1 Quantum computer and quantum gates

The concepts of quantum computing are borrowed and extended from classical computational theory. In the classical case, information is mostly represented in terms of binary digits, the so called bit, essentially mapping information to a base-2 number. Information processing is done with gates acting on those numbers. The idea of quantum computer is still to encode information in a binary form, but due to the nature of quantum mechanics, a quantum bit (in short qubit) gains new features that can be exploited to perform different kind of operations.

A qubit is formally a normalized wave function that can be written as superposition of two orthogonal states indicated usually with $|0\rangle$ and $|1\rangle$:

$$|\psi\rangle = \alpha|0\rangle + \beta|1\rangle, \quad (2.1.1)$$

where α, β are probability amplitudes, two complex numbers that satisfy the relationship $|\alpha|^2 + |\beta|^2 = 1$. At first glance, the advantage of qubits seems obvious, while one classical bit can store only one bit of information, a qubit can be in any linear combination, i.e. α and β can be chosen freely and any information can be represented. Although, the reality is different, due to rules of quantum mechanics, α and β cannot be directly accessed, which means that we can get only a limited amount of information out of a qubit. The outcome of measuring a qubit will give the value 0 with a probability of $|\alpha|^2$ and 1 with a

probability of $|\beta^2|$.

Qubits also have a geometrical representation that can be useful, equation (2.1.1) depends on 4 real numbers, however since ψ is normalized, we can rewrite the expression as

$$|\psi\rangle = e^{i\gamma} \left(\cos \frac{\theta}{2} |0\rangle + e^{i\varphi} \sin \frac{\theta}{2} |1\rangle \right). \quad (2.1.2)$$

the global phase factor $e^{i\gamma}$ can be left out, as it does not influence the measurement outcome. This leaves us with only two real number: θ and φ . A qubit is therefore representable with only these two numbers that we can chose to represent geometrically with normalized spherical coordinates. The so called Bloch sphere is depicted in figure 2.1.1, every point on its surface represents a different state of the qubit. Here qubit manipulation can be visualized as trajectories on the surface. The drawback of this representation is that it is limited to only one qubit, so it loses usefulness when dealing with multiple qubits.



Figure 2.1.1: The Bloch sphere. The states $|0\rangle$ and $|1\rangle$ are at the poles of the sphere, every other point of the surface represents a superpositions of these states. A quantum gate can be seen as trajectory on the surface mapping one state to another.

An alternative way of dealing with qubits is via matrices. We can assign to the states $|0\rangle$ and $|1\rangle$ the following:

$$|0\rangle = \begin{pmatrix} 1 \\ 0 \end{pmatrix} \quad |1\rangle = \begin{pmatrix} 0 \\ 1 \end{pmatrix} \implies |\psi\rangle = \begin{pmatrix} \alpha \\ \beta \end{pmatrix}. \quad (2.1.3)$$

In this representation, rotations of qubits are calculated using 2×2 unitary matrices. These kind of operations are named *quantum gates* and they are the building blocks of quantum computing. Quantum algorithm can be written as a sequence of quantum gates and it is therefore important to understand them. For a single qubit any gate can be written as combination of two operations [17]

$$U_z(\theta) = \begin{pmatrix} e^{-i\frac{\theta}{2}} & 0 \\ 0 & e^{i\frac{\theta}{2}} \end{pmatrix} \quad U_\varphi(\theta) = \begin{pmatrix} \cos \frac{\theta}{2} & -ie^{-i\varphi} \sin \frac{\theta}{2} \\ -ie^{i\theta} \sin \frac{\theta}{2} & \cos \frac{\theta}{2} \end{pmatrix}. \quad (2.1.4)$$

These two matrices can be seen as two different rotations in the Bloch sphere, U_z is a rotation around the z axis by the amount θ , while U_φ is a rotation on the $x - y$ plane around an axis tilted by φ . Important examples are the Hadamard gate H , which creates a superposition of one qubit starting from the state $|0\rangle$, or $|1\rangle$, and the phase shift gate R_ϕ that shift the phase:

$$H = \frac{1}{\sqrt{2}} \begin{pmatrix} 1 & 1 \\ 1 & -1 \end{pmatrix} \quad R_\phi = \begin{pmatrix} 1 & 0 \\ 0 & e^{i\phi} \end{pmatrix}. \quad (2.1.5)$$

As we have seen, a single qubit has already the advantage of superposition compared to classical case. When considering multiple qubits, we gain even more quantum mechanical features like entanglement. This phenomenon does not have a classical analogy and it is an extremely useful tools in quantum information.

In general a state with N qubits is written as tensor product of the single qubit states ψ_i

$$|\psi_N\rangle = |\psi_1\rangle \otimes |\psi_2\rangle \otimes \cdots \otimes |\psi_N\rangle \equiv |\psi_1\psi_2 \dots \psi_N\rangle. \quad (2.1.6)$$

If we had to write out explicitly all the probability coefficients of ψ_N , we would need 2^N complex numbers. It is clear then why classical computer cannot keep up. N bits can only give N^2 different combinations, while the Hilbert space of qubits is exponentially larger. Now, let us consider only 2 qubits, a particular case would be

$$|\psi\rangle = \frac{1}{\sqrt{2}} (|00\rangle + |11\rangle). \quad (2.1.7)$$

If a measurement is made on one of the two qubit and, for instance, the outcome is 0, the wave function collapses to the state $|00\rangle$, collapsing also the state of the other qubit, even if no operation has been directly performed on it. Next you measure the the second qubit and the outcome will be 0 with unit probability. Viceversa, if the outcome if the first measurement was 1, the state collapses to $|11\rangle$ and the outcome of the second measurement is always 1. The two qubits are correlated, but this correlations is stronger than the classical one.

Gates that involve multiple qubits are written as $2^N \times 2^N$ unitary matrices, a famous example is the controlled not (CNOT) gate

$$\text{CNOT} = \begin{pmatrix} 1 & 0 & 0 & 0 \\ 0 & 1 & 0 & 0 \\ 0 & 0 & 0 & 1 \\ 0 & 0 & 1 & 0 \end{pmatrix}. \quad (2.1.8)$$

It can be shown [15] that the examples of this section: H gate, phase gate, and CNOT gate form a universal set of quantum gates, i.e. a sequence of these gates approximates every other quantum gate.

2.1.2 Ion qubits and laser-ion interactions

Qubits can be encoded in any pair of orthogonal states. In the case of an ion it is possible to take two internal electronic states, the qubit is then implement in their transition. In figure 2.1.2 the level scheme of ${}^{40}\text{Ca}^+$ is presented. The lifetime of the excited level has to

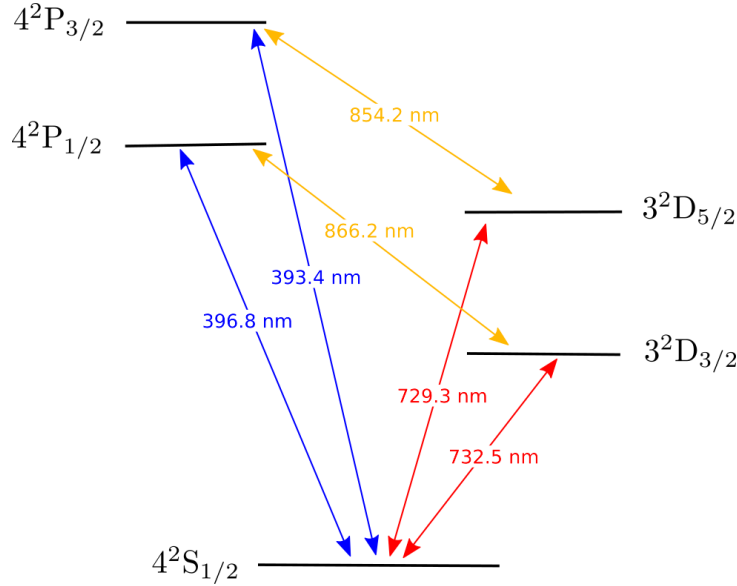


Figure 2.1.2: Level scheme of $^{40}\text{Ca}^+$. Detailed description is in section 3.1.1. For quantum computing purposes, the chosen qubit transition is the long lived quadrupole transition $|\text{S}_{1/2}\rangle \rightarrow |\text{D}_{5/2}\rangle$ at 729nm.

be long enough to carry out all the quantum operation without spontaneous scattering. A common choice is the transition $|\text{S}_{1/2}\rangle \rightarrow |\text{D}_{5/2}\rangle$, where the ground state $|\text{S}_{1/2}\rangle$ represents the state $|0\rangle$ and the excited state $|\text{D}_{5/2}\rangle$ will be $|1\rangle$. As these levels are separated by an optical frequency, this kind of qubit is often referred to as optical qubit. Lasers provide a way to directly manipulate the population of the two levels and therefore to manipulate the state of the qubit.

The interaction between ion and laser can be understood in terms of a simple model: a two-level atom with dipole interaction with laser field. Consider the system in figure 2.1.3, where the states $|0\rangle$ and $|1\rangle$ are separated by a frequency ω_0 , while the laser is assumed to be monochromatic with frequency ω_l . The difference $\Delta = \omega_l - \omega_0$ is called detuning and we assume to be in the near resonant regime $\Delta \ll \omega_0$. The laser light in this case can be described classically in the dipole approximation. This assumption can be explained as follow, the wavelength of transitions in an atom, are typically in the optical regime: hundreds of nanometers, which is order of magnitude greater than the typical atom dimension. Thus, the electric field can be considered constant over the atom size. This allows to expand the electric field in Taylor series and remove every spatial dependent term in the so called dipole approximation. The Hamiltonian of the atomic part can be written as:

$$H_a = \hbar\omega_0 |1\rangle \langle 1|, \quad (2.1.9)$$

where ω_0 is the frequency difference between the ground and excited state, the energy of the ground state has also been set to 0. The Hamiltonian of the interaction between the dipole atomic moment d and the electric field of the laser can be written [18]

$$H_{int} = -d \cdot E \quad (2.1.10)$$

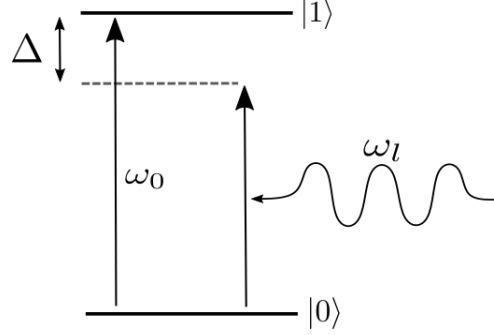


Figure 2.1.3: 2-level atom scheme, the ground and excited states are denoted as $|0\rangle$, and $|1\rangle$. ω_l is the laser frequency, which is detuned by $\Delta \equiv \omega_l - \omega_0$ from the transition frequency ω_0 .

where the electric field will be treated classically and the dipole approximation is assumed. This means

$$E(t) = \hat{\varepsilon} E_0 \cos(\omega t + \varphi) = \hat{\varepsilon} \frac{E_0}{2} (e^{-i(\omega t + \varphi)} + e^{i(\omega t + \varphi)}), \quad (2.1.11)$$

where ε is a the unit polarization vector. The next step is to work out the dipole operator, this can be done by applying the identity $|0\rangle\langle 0| + |1\rangle\langle 1|$ on both sides of d . Due to parity arguments [18], only the non diagonal terms are non vanishing, giving

$$d = \langle 0|d|1\rangle (|0\rangle\langle 1| + |1\rangle\langle 0|) \equiv \langle 0|d|1\rangle (\sigma + \sigma^\dagger). \quad (2.1.12)$$

Combining the last three equations yields

$$H_{int} = -\langle 0|\hat{\varepsilon}d|1\rangle \frac{E_0}{2} (\sigma e^{i(\omega_l t + \varphi)} + \sigma^\dagger e^{-i(\omega_l t + \varphi)} + \sigma e^{-i(\omega_l t + \varphi)} + \sigma^\dagger e^{i(\omega_l t + \varphi)}) \quad (2.1.13)$$

A rotating wave approximation is used now, essentially σ (σ^\dagger) evolves in time as $\propto e^{-i\omega_0 t}$ ($\propto e^{i\omega_0 t}$), therefore we can drop the fast oscillating terms in the last equation and keeping only those that depends on time as $\propto e^{\pm i(\omega_l - \omega_0)t}$. The validity of this approximation is given by the facts that ω and ω_0 are in the optical regime, thus they oscillate extremely fast and average to zero, the interesting slow dynamic is given only by their difference, aka detuning. With this approximation we arrive at the final form of the interaction Hamiltonian

$$H_{int} = \frac{\hbar\Omega}{2} (\sigma e^{i(\omega_l t + \varphi)} + \sigma^\dagger e^{-i(\omega_l t + \varphi)}), \quad (2.1.14)$$

where we defined the Rabi frequency $\Omega \equiv -\langle 0|\hat{\varepsilon}d|1\rangle E_0/\hbar$. The Rabi frequency depends linearly with the applied electrical field and hence its square is proportional to the intensity of the laser $\Omega^2 \propto I$. To summarize, the final system Hamiltonian is

$$H = H_a + H_{int} = \hbar\omega_0 |1\rangle\langle 1| + \frac{\hbar\Omega}{2} (\sigma e^{i(\omega_l t + \varphi)} + \sigma^\dagger e^{-i(\omega_l t + \varphi)}). \quad (2.1.15)$$

This Hamiltonian depends explicitly on time, which could lead to unnecessary complications if we want to solve the dynamics. To eliminate the time dependence, we can go in the rotating frame with the unitary transformation $U = e^{i\omega_l t |1\rangle\langle 1|}$, the Hamiltonian in this frame is

$$\tilde{H} = -\hbar\Delta |1\rangle\langle 1| + \frac{\hbar\Omega}{2} (e^{i\varphi}\sigma + e^{-i\varphi}\sigma^\dagger) \quad (2.1.16)$$

The time dependence is now gone, and the unitary evolution matrix can be calculated as

$$U(t) = \exp \left\{ -\frac{i}{\hbar} \tilde{H}t \right\} = \begin{pmatrix} \cos \left(\frac{\tilde{\Omega}t}{2} \right) + i \frac{\Delta}{\tilde{\Omega}} \sin \left(\frac{\tilde{\Omega}t}{2} \right) & -ie^{i\varphi} \frac{\Omega}{\tilde{\Omega}} \sin \left(\frac{\tilde{\Omega}t}{2} \right) \\ -ie^{-i\varphi} \frac{\Omega}{\tilde{\Omega}} \sin \left(\frac{\tilde{\Omega}t}{2} \right) & \cos \left(\frac{\tilde{\Omega}t}{2} \right) - i \frac{\Delta}{\tilde{\Omega}} \sin \left(\frac{\tilde{\Omega}t}{2} \right) \end{pmatrix}. \quad (2.1.17)$$

Where $\tilde{\Omega} = \sqrt{\Delta^2 + \Omega^2}$ is the generalized Rabi frequency. With this matrix we can calculate all the dynamic we need. In the case of zero detuning $\Delta = 0$, we also notice that the matrix is the same as equation (2.1.4). Thus, a resonant laser pulse implements the qubit rotation $U_\varphi(\theta)$, the rotation around the z axis is performed with a laser pulse as well, but far detuned from the transition. We will explore this possibility later in the AC Stark shift.

As example, let us take the atom in the ground state $|\psi\rangle = |0\rangle$ and apply the unitary evolution (2.1.17). The probability to be in the excited state becomes

$$\mathbb{P}\{|1\rangle\}(t) = |\langle 1|U(t)|0\rangle|^2 = \frac{\Omega^2}{\Omega^2 + \Delta^2} \sin^2 \left(\frac{\tilde{\Omega}t}{2} \right) \quad (2.1.18)$$

This equation is plotted in figure 2.1.4. For $\Delta = 0$, we get a cosine behaviour, the so called Rabi oscillations. The probability amplitude for the electron, under continuous drive by a laser, will oscillate between the ground and excited state at a frequency Ω . Detuning damps the amplitude of such oscillations and increases the oscillation frequency. Rabi oscillations are an important tool in quantum information, laser pulses can prepare the state of the qubit in any superposition, e.g. starting in the $|0\rangle$ state, a $\pi/2$ pulse ($\Omega t = \pi/2$ and phase $\varphi = 0$) will result in the state $(|0\rangle - i|1\rangle)/\sqrt{2}$, with a π pulse ($\Omega t = \pi$, $\varphi = \pi$) the population is completely transferred to another level $|0\rangle \rightarrow |1\rangle$. These pulses can be used to implement the Hadamard gate of equation (2.1.5).

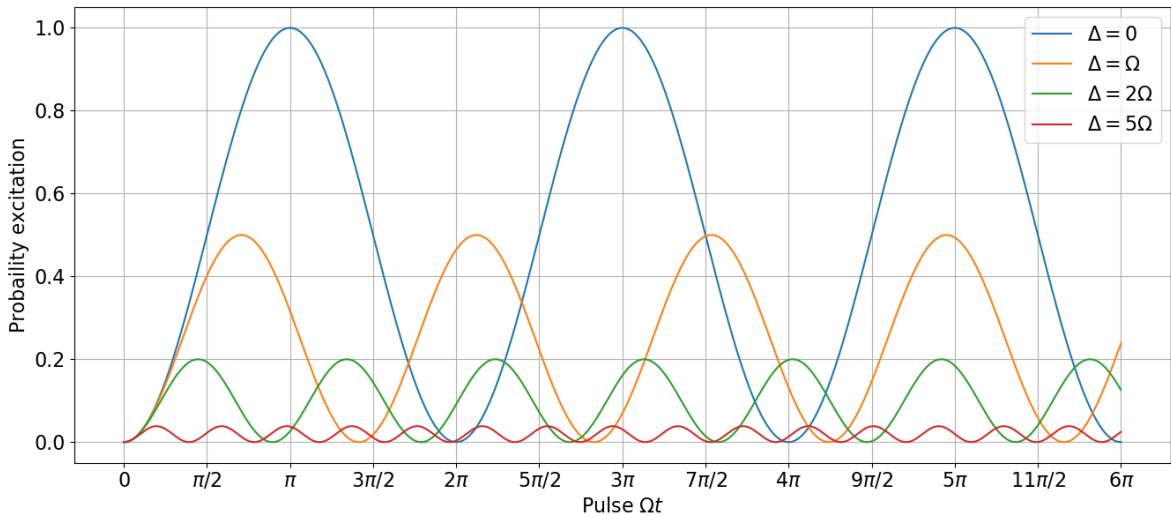


Figure 2.1.4: Rabi flops for different detuning Δ

As the light is detuned from the transition, Rabi oscillations are suppressed: the amplitude is reduced by a factor of 0.5 already with $\Delta = \Omega$, while a factor of 10 in reduction is achieved with a detuning of $\Delta/\Omega = 5$. However, another effect persists in the off-



Figure 2.1.5: 3 level atom model. Two long lived ground states $|g_1\rangle$, $|g_2\rangle$ couple to an excited level $|e\rangle$ through two laser of frequencies ω_1 , ω_2 detuned respectively Δ_1 , Δ_2 from the transition.

resonant regime: the energy levels are shifted. The shift δ can be calculated by finding the eigenvalues of the Hamiltonian (2.1.16), which can be written in matrix form and diagonalized. We find that there are two eigenstates $|+\rangle$ and $|-\rangle$ called dressed states with eigenvalues

$$E_{\pm} = -\frac{\hbar\Delta}{2} \pm \frac{\hbar}{2}\sqrt{\Delta^2 + \Omega^2}. \quad (2.1.19)$$

In the limit $\Delta \gg \Omega$, dressed states tend to the bare states $|+\rangle \rightarrow |1\rangle$, $|-\rangle \rightarrow |0\rangle$, and the energies becomes

$$E_{\pm} \rightarrow -\frac{\hbar\Omega}{2} \pm \frac{\hbar\Omega}{2} \pm \frac{\hbar\Omega^2}{4\Delta} \implies \delta = \pm \frac{\Omega^2}{4\Delta}. \quad (2.1.20)$$

The effective Hamiltonian for the off-resonant regime can be derived following a Markovian approximation [19]

$$H_{AC} = \frac{1}{\hbar\Delta} [\sigma, \sigma^\dagger] = \frac{\hbar\delta}{2} \sigma_z \quad (2.1.21)$$

The corresponding evolution is

$$U(t) = \exp \left\{ -\frac{i}{\hbar} H_{AC} t \right\} = \begin{pmatrix} \exp \left\{ i \frac{\delta}{2} t \right\} & 0 \\ 0 & \exp \left\{ -i \frac{\delta}{2} t \right\} \end{pmatrix}. \quad (2.1.22)$$

This matrix implements the quantum gate from equation (2.1.4). Furthermore, Ac Stark shift can also implement the phase gate R_ϕ of equation (2.1.5), but it requires a third energy level.

2.1.2.1 Three-level model

We extend our model to a 3 level Λ type atom, which closer resemble the real experimental system, driven by two lasers. The model is more complex but contains new effects that explain photon generation and qubit gates. In particular, stimulated Raman transition will be discussed, and we will show how, under certain conditions, the system can be approximated as an effective 2 level atom. The system is depicted in figure 2.1.5, two ground states $|g_1\rangle$ and $|g_2\rangle$ are present together with a common excited state $|e\rangle$. Two different lasers drive the transition $|g_1\rangle \rightarrow |e\rangle$ and $|g_2\rangle \rightarrow |e\rangle$ with detuning Δ_1 and Δ_2 . In

the case of calcium, the ground states are $|S_{1/2}\rangle$, and $|D_{5/2}\rangle$. This is the qubit transition, and it is long lived, such that any spontaneous emission between S and P can be neglected. The excited level is $|P_{3/2}\rangle$ which can decay into both ground states.

In this model we assume that the two ground states are not separated by an optical frequency $\omega_{02} - \omega_{01} \ll \omega_1, \omega_2$, and that the detunings are nearly equal $\Delta_1 \simeq \Delta_2$. As a consequence, each laser light couples only to one transition.

The mathematical description is similar to the one described in section 2.1.2 for the 2 level atom with the addition of extra terms. The bare atom Hamiltonian is

$$H_a = -\hbar\omega_{01}|g_1\rangle\langle g_1| - \hbar\omega_{02}|g_2\rangle\langle g_2|, \quad (2.1.23)$$

with the convention of setting the excited level energy to 0. The electric field is now the sum of the two lasers lights

$$E(t) = \hat{\varepsilon}_{01}E_{01}\cos(\omega_1 t \varphi_1) + \hat{\varepsilon}_{02}E_{02}\cos(\omega_2 t + \varphi_2). \quad (2.1.24)$$

We still apply the dipole and the rotating wave approximation to the interaction between electric field and atom. Finally transforming into the rotating frame gives the full final Hamiltonian as [18]

$$H = \hbar\Delta_1|g_1\rangle\langle g_1| + \hbar\Delta_2|g_2\rangle\langle g_2| + \frac{\hbar\Omega_1}{2}\left(\sigma_1e^{i\varphi_1} + \sigma_1^\dagger e^{i\varphi_1}\right) + \frac{\hbar\Omega_2}{2}\left(\sigma_2e^{i\varphi_2} + \sigma_2^\dagger e^{i\varphi_2}\right), \quad (2.1.25)$$

where $\Omega_i = -\frac{\langle g_1 | \varepsilon_i \cdot d | e \rangle E_i}{\hbar}$, and $\sigma_i = |g_i\rangle\langle e|$.

2.1.2.2 Dissipative processes

2.2 Quantum networking with trapped ions

2.2.1 General introduction

A quantum network is a collection of quantum processors, called nodes, interconnected with quantum channels. Quantum channels have the unique property to be able to transmit quantum state among the nodes and distribute entanglement over the network [20]. There are two classes of quantum networks which are differentiated by the purpose, networks can be used for transmission of information, i.e. communication, or for distributed quantum computation, i.e. scaling of quantum processors [21]. In these two cases the topology of the network is different, but the core elements are the same: a node, where quantum information is prepared, manipulated, and stored; and a link that connects nodes. Links can be realized in free space [22] or with optical fibers, photons can carry quantum information over long distance with high speed. Nodes can be realized using different physical systems: trapped ions [21], neutral atoms [23], atomic ensembles [20]. Nodes and links are connected through an interface that converts a stationary qubit in a node to a flying qubit over the network. In the next section we will explore how an interface can be realized by placing an ion based quantum memory in an optical cavity.

For a fully deployed quantum network, many challenges have to be faced. Faithful transmission of a quantum states over long distances can be a daunting problem as quantum information cannot be cloned [24], and noisy channels can destroy the delicate

nature of qubits. Quantum repeaters have been designed [25] to circumvent these problems through a series of protocols which includes error corrections, or entanglement purification [26]. More protocols are also available to entangle qubits located in spatially separated quantum nodes [27]. Once entanglement has been established between nodes, other network functionalities become available, like for instance teleportation [28]. Entanglement generation, and quantum repeaters are just some examples of the fundamental steps necessary for building a quantum network, for a more in depth review look at [4].

2.2.2 Cavity QED

Trapped ions can become quantum nodes of a quantum network by placing them in a cavity. Ions emits photon by spontaneous emission, or stimulated emission. The problem with spontaneous emission is that the photonic channel of emission is random and in free space. To realize a quantum interface, photon should be produced almost deterministically in defined mode. The trick is to use a cavity tuned to one particular transition, such that the probability of a photon to be emitted in the cavity mode is greatly enhanced. In this section we describe a simple model of a two-level system in a cavity, the derivation is similar to section 2.1.2, with the difference that in a cavity the electric field is quantized. Using the mode operator a, a^\dagger the electric field inside a cavity can be written as:

$$E = A(f(r)a + f^*(r)a^\dagger) \quad (2.2.1)$$

where A is an amplitude, and $f(r)$ is the spatial mode profile [29]. The interaction between the field and the cavity is obtained as from $H_{int} = -d \cdot E$, following a rotating wave approximation the result is

$$H_{int} = \hbar g(\sigma a^\dagger + \sigma^\dagger a), \quad (2.2.2)$$

where $g = A \langle g|d|e \rangle f(r)$ is called cavity coupling constant. It is analogous to the Rabi frequency, it gives an idea of the coupling between the cavity field and the 2-level atom. An important dependence of g can be found by considering that $f(r)$ is inversely proportional to the volume of the cavity V , i.e.

$$g \propto \langle g|d|e \rangle \sqrt{\frac{\omega}{2\varepsilon_0 \hbar V}}. \quad (2.2.3)$$

The coupling therefore, increases with decreasing cavity volume and viceversa. The total system Hamiltonian includes also the atomic part, and a single mode optical field. It takes the name of Jaynes-Cummings Hamiltonian and it is written as [30]

$$H = \hbar\omega_0 |1\rangle\langle 1| + \hbar\omega a^\dagger a + \hbar g(\sigma a^\dagger + \sigma^\dagger a). \quad (2.2.4)$$

States now are a product state of the atomic part and the photon number $|g, n\rangle, |e, n\rangle$. They are however not the eigenstates of the Jaynes-Cummings Hamiltonian. It can be seen that this Hamiltonian is block diagonal, which means that each 2×2 block can be diagonalized, the dressed states found after diagonalization are similar to the semiclassical model. Moreover, also the dynamics is analogue to the semiclassical case, Rabi oscillations are still present with quantized Rabi frequency given by $\Omega_n = \sqrt{4(n+1)g^2 + \Delta^2}$.

The presence of a cavity makes dynamics more interesting, especially when considering

spontaneous emission and interaction with cavity modes. For a mathematical description, we need to introduce dissipative process that do not follow an Hermitian evolution. This is done heuristically by adding terms in the Heisenberg equation

$$\frac{d\rho}{dt} = \frac{1}{i\hbar}[H, \rho] + \mathcal{L}(\rho). \quad (2.2.5)$$

This equation is usually referred to as master equation in Lindblad form, where ρ is the density matrix of system. The superoperator $\mathcal{L}(\rho)$ contains phenomena not included in the Hamiltonian. In our case, we are most interested in two process: spontaneous emission in a free space field mode, and decay in one cavity mode and out of the cavity. The first is quantified with the decay rate Γ , while the latter is characterized by the decay rate κ . The functional dependence of these two terms goes as [18]

$$\mathcal{L}(\rho) = \Gamma\mathcal{D}(\sigma)\rho + \kappa\mathcal{D}(a)\rho. \quad (2.2.6)$$

A good approximation of the model is given in the *strong coupling* regime $g \ll \Gamma, \kappa$, where damping due to dissipative process is slow and dynamics is mainly driven coherently by the coupling atom-cavity g . The decay rate κ depends exclusively on the cavity parameters as [29]

$$\kappa = \frac{c\pi}{FL}, \quad (2.2.7)$$

where F is the cavity finesse, and L the length. In the design of the experiment one must play and compromise with these three parameters in order to reach a good coupling ion-cavity but also being able to send photons out of the cavity.

2.2.3 Photon generation

By placing a cavity around the trap, photon generation is enabled. The cavity mediated Raman process is responsible for this phenomenon. It can be explained strating from a three level atom like in figure 2.2.1. The electron is initially in the ground state $|0\rangle$, a laser pulse excite the transition $S_{1/2} \rightarrow D_{3/2}$ detuned properly to eliminate the population in the $|1\rangle$ level. Among the decay channels of the electron, the decay $P_{3/2} \rightarrow D_{5/2}$ is enhanced due to the presence of the cavity and therefore the coupling g between the ion and the cavity mode. The electron will more likely decay to the $D_{5/2}$ state emitting a photon inside the cavity. Thus the process can be described as $|0\rangle_i |0\rangle_p \rightarrow |1\rangle_i |1\rangle_p$ where the subscript i indicates the ion and p the photon number in the cavity. The detuning is set such as $\Delta \gg \Omega, g$, in this regime the whole process can be described as a single transition with effective Rabi frequency of [29]

$$\Omega_{eff} = \frac{\Omega g}{2\Delta}. \quad (2.2.8)$$

It is equivalent of a classical Raman process driven with two laser pulses on the two different transitions, but in this case the second laser is substituted by the vacuum standing wave of the cavity. In order to avoid decay in other channels, one must be sure that Ω_{eff} is larger than the effective decay rate of other spontaneous emission $\Omega_{eff} \gg \Gamma_{eff}$. Moreover, the photon should leave the cavity after the transfer is complete, this is ensured by $\Omega_{eff} > \kappa$.

In the real case the electronic states are also shifted due to a magnetic field generated

by a permanent magnet perpendicular to the cavity axis and at 45° with respect to the trap axis. This is done in the optics of achieving ion-photon entanglement, since in that case multiple Zeeman levels should be addressed. The situation is therefore further complicated and the polarization of the laser field should be taken into consideration. In figure (), the Zeeman structure of $^{40}\text{Ca}^+$ is depicted. One can start from the state $|\text{S}_{1/2}, m_j = -1/2\rangle$. From here three choices of polarization can be taken: σ^- , π , σ^+ , for each choice three Raman transition are possible, the most favorable in the case of the magnetic field orthogonal to the cavity axis is [14]

$$|\text{S}_{1/2}, -1/2\rangle \rightarrow |\text{P}_{3/2}, -3/2\rangle \rightarrow |\text{D}_{5/2}, -5/2\rangle. \quad (2.2.9)$$

In this case the transitions strengths, i.e. the projection on the laser polarization onto the dipole moment, and the same projection onto the cavity axis are maximized.

The generated photon from this process can be entangled with the ion state by driving this Raman transition with a bichromatic beam. This means that the laser pulse drives two transitions at the same time, for example the one that ends up in $|\text{D}_{5/2}, -5/2\rangle$ and $|\text{D}_{5/2}, -3/2\rangle$. In this instance, the generated photon will be a superposition of σ^+ and π polarization. With respect to the cavity it means vertical and horizontal polarization. The final state of the bichromatic transition is therefore

$$|\psi\rangle = |\text{D}_{5/2}, -5/2\rangle |H\rangle + |\text{D}_{5/2}, -3/2\rangle |V\rangle. \quad (2.2.10)$$

In the real experiment the designed cavity is near concentric with a length of 19.9 mm, and radii of curvature of 9.98 mm. The cavity length is actively stabilized with a PDH type feedback which locks the mirrors position to a 806nm laser. One mirror of the cavity is highly reflective $T_1 = 2.2$ ppm, while the other is more transmissive $T_2 = 97$. This asymmetry of the mirrors allows for the produced photons to exit one from one side in most cases and subsequently coupled to a fiber. The probability to get a photon out of the cavity from the designed mirror can be determined from the transmission and losses of the cavity, the maximum achievable is $P_{max} = 0.83$. The maximum g factor achievable with this geometry is $g = 2\pi \times 1.53$ MHz.

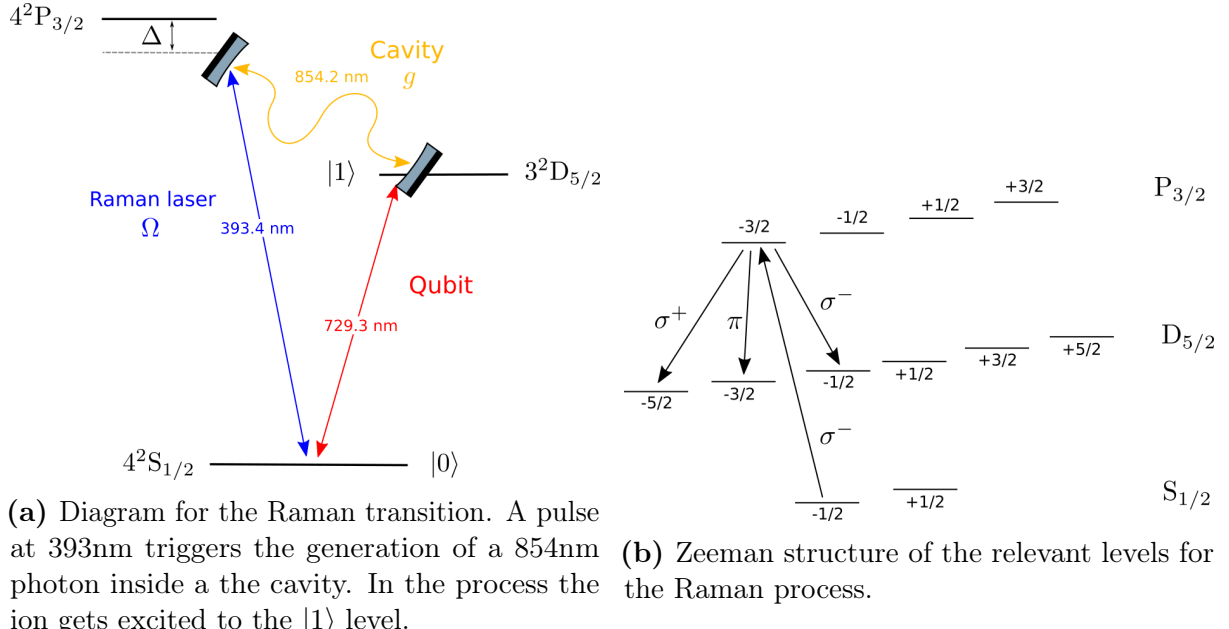


Figure 2.2.1

The Finesse of the cavity for the TEM_{00} mode is 54000. The other cavity parameters are $\kappa = 2\pi \times 70$ kHz, and $\gamma = 2\pi \times 11.45$ MHz for the $P_{3/2}$ state. With these numbers the preferred strong regime is not reached, but nonetheless, it is still possible to produce photons and collect them out of the cavity.

2.3 Basics of ion trapping

2.3.1 Linear Paul trap

In order to trap a charged atom, a three dimensional trapping potential ϕ is needed. However it follows directly from Maxwell equation $\nabla^2\phi = 0$ that the potential must be antitrapping at least in one direction. There are two workarounds for this problem: the first one introduces magnetic fields to trap particles in some directions, this takes the name of Penning trap. The second solution is the so called Paul trap, and it is what we are going to describe in this section. The idea is to introduce a time varying potential, such that the antitrapping direction is constantly switching between two different dimension. If the switching is timed correctly, the particle will not have the time to escape but will always encounter a potential barrier. The shape of the trap can be adapted to load more ions in different geometries. For instance, a linear Paul trap is elongated in one direction where the trapping confinement is weaker, such that loaded ions will align in a single long string. This kind of trap is depicted in figure 2.3.1.

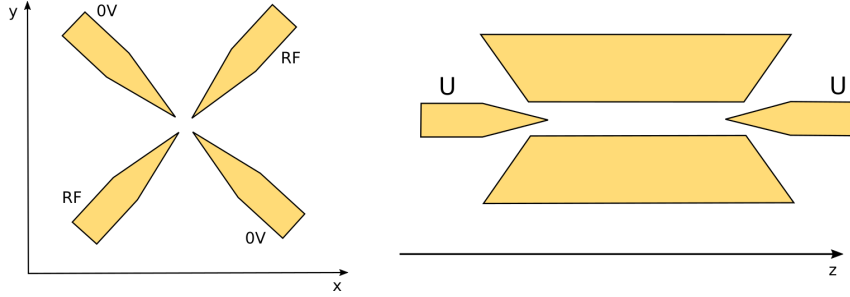


Figure 2.3.1: A linear Paul trap. U is the voltage applied to the electrodes trapping in the z direction, while in the $x - y$ plane trapping is achieved with a radio frequency signal. r_0 is the distance from the central axis to the RF electrodes.

The confinement in the $x - y$ plane is provided by 4 electrodes, two of which are grounded and the other two are connected to a radio frequency source. This design is similar to a mass filter, with the difference of additional endcaps electrodes in the z direction that plug the trap and confine also in axial direction.

The potential inside the trap can be described for the $x - y$ plan independently from the z direction. In the case of a linear Paul trap the radial potential is [31]:

$$\phi = \frac{\Phi_0}{2r_0^2} (x^2 - y^2), \quad (2.3.1)$$

with the amplitude that consists of a static part U and a dynamical one $\Phi_0 = U + V \cos(\Omega_{RFT})$. The study of the particle's motion with mass m and charge e inside the trap can be done with classical physics, Newton's second law in this case is

$$m\ddot{x} = -q \frac{\partial \phi}{\partial x} = -\frac{ex}{r_0^2} (U + V \cos(\Omega_{RFT})), \quad (2.3.2)$$

and similarly for \ddot{y} . This equation can be written in the form of Mathieu equation by defining two parameters:

$$a_x = \frac{4eU}{\Omega_{RF}^2 r_0^2 m}, \quad q_x = \frac{2eV}{\Omega_{RF}^2 r_0^2 m} \implies \ddot{x} + \frac{\Omega_{RF}}{4} (a_x + 2q_x \cos(\Omega_{RF}t)) x = 0 \quad (2.3.3)$$

and with a change of variable $\tau = \frac{\Omega_{RF}t}{2}$ we end up with

$$\frac{\partial^2 x}{\partial \tau^2} + (a_x + 2q_x \cos(2\tau)) x = 0 \quad (2.3.4)$$

This kind of equations have stable solutions that can be found in a recursive way with Floquet theorem [32]. However, the problem is simplified by performing the so called secular approximation, which consists of separating the motion in a slow changing position: \bar{x} called *secular motion*, and in a rapid oscillation: ξ , called *micromotion*. The behaviour of micromotion is dictated by the force due to the potential at the position \bar{x} , and the secular motion will follow a time average of the potential $\langle \phi(t) \rangle$ eliminating therefore the effect of micromotion. In this case, equation (2.3.4) can be solved in the limit $a_x \ll q_x \ll 1$

$$x(t) = x_0 \cos(\omega_x t + \phi_x) \left[1 + \frac{q_x}{2} \cos(\Omega_{RF}t) \right]. \quad (2.3.5)$$

Where we recognize a slowly varying oscillation with amplitude modulated by a faster oscillation. The approximation is valid only in the case $\omega_x \ll \Omega_{RF}$. The frequency ω_x is given in the solution as

$$\omega_x = \frac{\Omega_{RF}}{2} \sqrt{a_x + \frac{q_x^2}{2}}. \quad (2.3.6)$$

By imposing real solution, the stability diagram of the trap can be found. It is depicted in figure 2.3.2. The other spatial dimension can be treated in the same way and the results are the same. Important to notice is that a consequence of the secular approximation is that the potential can be approximated, the ion in the trap sees therefore a pseudo potential which is harmonic. Deviations from harmonicity are possible and they are mainly due to stray fields. Extra electrodes can be added to the trap design to compensate for such deviations.

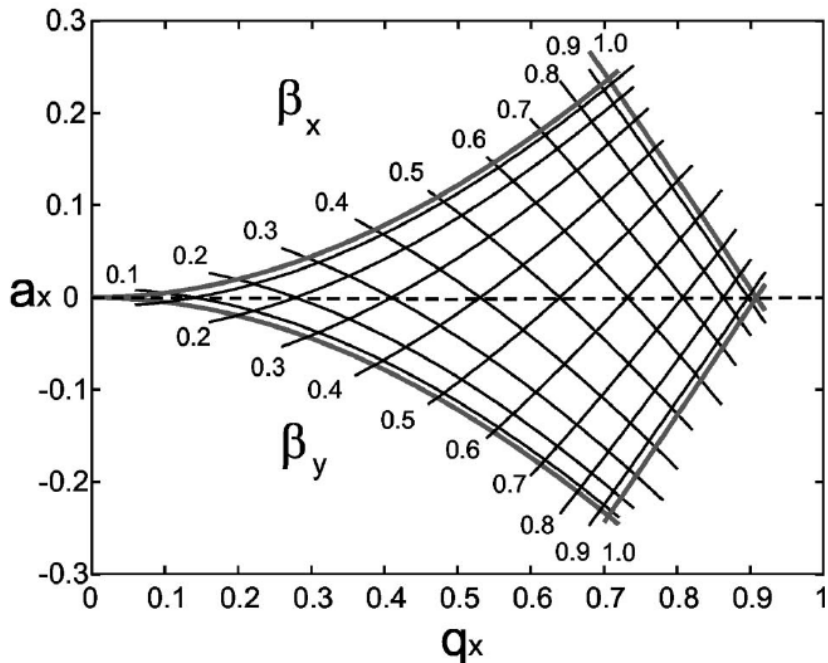


Figure 2.3.2: Stability diagram for a linear Paul trap, taken from [32]. The coefficient β_x, β_y can be calculated numerically from a_x and q_x

2.3.2 Ion strings

We have seen that the potential inside the trap can be described as an harmonic potential. What we are interested in, is the ion separation between N ions loaded in the trap. This will give us an idea of how narrowly the beam should be focused and will set an appropriate problem spatial scale.

Let us consider the z direction where the ions are weakly confined and will form a string. The potential can be approximated as harmonic and hence given by

$$V = \sum_{i=0}^N \frac{1}{2} M \omega^2 z_i^2 + \sum_{i \neq j}^N \frac{Z^2 e^2}{8\pi\epsilon_0} \frac{1}{|z_i - z_j|} \quad (2.3.7)$$

The equilibrium position can be found at the minima of the potential, i.e. where the first derivative zeros

$$\frac{\partial V}{\partial z_i} = 0 \implies u_i - \sum_{j=1}^{i-1} \frac{1}{(u_i - u_j)^2} + \sum_{j=i+1}^N \frac{1}{(u_i - u_j)^2} = 0, \quad (2.3.8)$$

where we defined the dimensionless quantity $u_i = z_i/l$ and $l^3 = \frac{Z^2 e^2}{4\pi\epsilon_0 M \omega^2}$. The last equations can be solved analytically only for 2 or 3 ions. In fact, for the case $N = 2$ we simply get the system

$$\begin{cases} u_1 + \frac{1}{(u_1 - u_2)^2} = 0 \\ u_2 - \frac{1}{(u_1 - u_2)^2} = 0 \end{cases} \implies u_1 = -u_2, \quad u_1 = \left(\frac{1}{2}\right)^{2/3} \simeq 0.629 \quad (2.3.9)$$

For calcium-40 ions in a Paul trap with axial confinement of $\omega = 1$ MHz, we have $l \simeq 4.45 \times 10^{-6}$ m, which means that 2 ions are separated by $\simeq 5.6$ μ m. In the case of more ions the separation is lesser with the same confinement, but it is also possible to lower the axial frequency and increase the separation between the ions such that also in the case of several ions, the distance between them is still in the order of several μ m. This size is accessible with current focusing optics and it is above the diffraction limit.

For more ions, a numerical approach has to be used, [33] reports values of u_i up to $N = 10$, and gives an empirical formula of the minimum separation

$$u_{min}(N) \simeq \frac{2.018}{N^{0.559}}, \quad (2.3.10)$$

Although, numerical solution are preferred and can be computed fast.

2.3.3 Doppler cooling and detection

Ion trapping was treated here classically, because ions, when trapped, are still hot and follow classical mechanics. In order to reach the quantum regime, they must be cooled down. Several techniques are available for cooling, but the most popular and more frequently used is doppler cooling. The idea comes from neutral atoms and can be applied to ions as well: a laser interacts with a particular transition, exchanging a photon and therefore giving a momentum kick $\Delta p = \hbar \mathbf{k}$ in a particular direction to the ion. The absorbed photon is given back through spontaneous emission in a random direction, giving another kick to the ion. Over many cycles of absorption and emission, the random kick due to emission will average to zero, while the kick given by the laser will accumulate slowing down and cooling the ion in the direction of the laser.

The difference with neutral atoms is that an ion is confined inside a trap rotating at frequency ω . Hence, even the simple 2-level system gains new transitions called sidebands. Some consideration must be put into the relative strength of the decay rate Γ with respect to the sidebands. For describing the Doppler cooling we assume that the ion is weakly confined $\omega \ll \Omega$. The intuitive picture is that the rate of spontaneous emission in this case is much faster than the time scale over which the trap changes potential. Therefore, the trap can be considered static and has no effect on the cooling.

In order to describe spontaneous emission, we use the master equation (2.2.5), in the case

of spontaneous emission, the superoperator is given by [34]

$$\mathcal{L}(\rho) = \frac{\Gamma}{2} (2\sigma\rho\sigma^\dagger - \{\sigma^\dagger\sigma, \rho\}). \quad (2.3.11)$$

Γ is the decay rate from the excited state to the ground state. The actual value is found in perturbation theory with Fermi's golden rule []

$$\Gamma = \frac{\omega_0^3}{3\pi\varepsilon_0\hbar c^3} |\langle e|d|g\rangle|^2 \quad (2.3.12)$$

The master equation (2.2.5) can be explicitly written for every component of the density matrix ρ , in the rotating frame they are called optical equations and they are

$$\frac{d\rho_{ee}}{dt} = -i\frac{\Omega}{2}(\rho_{eg} - \rho_{ge}) - \Gamma\rho_{ee} \quad (2.3.13)$$

$$\frac{d\rho_{gg}}{dt} = i\frac{\Omega}{2}(\rho_{eg} - \rho_{ge}) + \Gamma\rho_{ee} \quad (2.3.14)$$

$$\frac{d\rho_{ge}}{dt} = -\left(\frac{\Gamma}{2} + i\Delta\right)\rho_{ge} - i\frac{\Omega}{2}(\rho_{ee} - \rho_{gg}) \quad (2.3.15)$$

$$\frac{d\rho_{eg}}{dt} = -\left(\frac{\Gamma}{2} - i\Delta\right)\rho_{eg} + i\frac{\Omega}{2}(\rho_{ee} - \rho_{gg}) \quad (2.3.16)$$

The most interesting solution is the population of the excited level ρ_{ee} in the steady state case, i.e. when the system reached equilibrium. In this case we look at $\rho_{ee}(t \rightarrow \infty)$, the solution of equation (2.3.13) is

$$\rho_{ee}(t \rightarrow \infty) = \frac{\Omega^2/\Gamma^2}{1 + \left(2\frac{\Delta-\mathbf{k}\cdot\mathbf{v}}{\Gamma}\right)^2 + 2\frac{\Omega^2}{\Gamma^2}} \quad (2.3.17)$$

The force exerted on the ions, due to the radiative pressure, is proportional to this population as

$$F = \hbar k \Gamma \rho_{ee} \simeq F_0 + \frac{dF}{dv} v = \hbar k \Gamma \frac{\Omega^2}{\Gamma^2 + 4\Delta^2} + F_0 \frac{8k\Delta}{\Gamma^2 + 4\Delta^2} v \quad (2.3.18)$$

where we assumed low velocities $v \simeq 0$ and thus linearized the equation. The effect of the constant term in the force is just to displace the ion from its central position. Instead, the linear term acts as a viscous friction that cools the ions with a rate of $\dot{E}_c = \langle Fv \rangle$. If on one side spontaneous emission allows for Doppler cooling, it also sets the lower limit. The small fluctuations in the Brownian motion leads to diffusion which heats the ion at a rate of

$$\dot{E}_h = \frac{1}{m} \frac{d}{dt} \langle p^2 \rangle = \frac{1}{m} (\hbar k)^2 \Gamma \langle \rho_{ee}(v) \rangle. \quad (2.3.19)$$

At equilibrium, the heating rate equals the cooling rate giving the lowest temperature achievable

$$\dot{E}_h + \dot{E}_c = 0 \implies k_B T = -\frac{\hbar\Gamma}{4} \left(\frac{\Gamma}{2\Delta} + \frac{2\Delta}{\Gamma} \right). \quad (2.3.20)$$

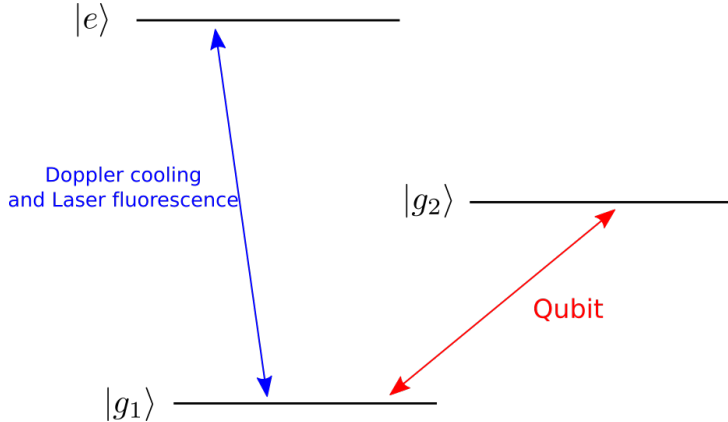


Figure 2.3.3: Λ type scheme. Two ground states $|g_1\rangle$ and $|g_2\rangle$ are stable or metastable, while the excited level $|1\rangle$ is short lived. Qubit is encoded in the two ground states while laser fluorescence and laser cooling is done on the $|g_1\rangle \rightarrow |1\rangle$ transition.

From here it is clear that by choosing the appropriated detuning, it is possible to reach the lowest temperature

$$T_{min} = \frac{\hbar\Gamma}{2k_B}, \quad \text{for } \Delta = -\frac{\Gamma}{2} \quad (2.3.21)$$

The achieved temperatures with Doppler cooling are enough to perform standard measurements. To go further down in temperature, sideband cooling is used, here particular sideband transition are excited to reduce the phonon number of the ions inside the trap.

With the same interaction of Doppler cooling, state detection can also be performed by means of laser induced fluorescence. Consider the Λ scheme in figure 2.3.3, the qubit is encoded in the level $|g_1\rangle$ and $|g_2\rangle$. To distinguish in which state the electron is, the transition $|g_1\rangle \rightarrow |1\rangle$ is excited. In the case the electron is in $|g_1\rangle$, the electron undergoes Rabi flops and scatters photons that can be collected and measured. If the electron is $|g_2\rangle$, no photons will be emitted and therefore no light is collected. The difference between these bright and dark states is clear and detection can be performed efficiently with near perfect efficiency.

In the real case, one must take into consideration also all the other levels. In fact, an electron from the excited state $|1\rangle$ can have multiple decay channels to other states and repumping becomes necessary.

2.4 Laser beam

2.4.1 Gaussian beams

Lasers emit light in the shape of Gaussian beams, so it is import to understand what Gaussian beams are and their characteristics. In this chapter we will take a closer look into such beams and introduce important quantities to characterize a Gaussian beam.

From a theoretical point of view, Gaussian beams are solution of the Helmholtz equation $(\nabla^2 + k^2)U(r) = 0$, with k being the wavevector. Such equation is a time independent variant of the wave equation that follows directly from Maxwell equations. A paraxial approximation is often used, i.e. we assume that the amplitude $A(r)$ of the wave is slowly

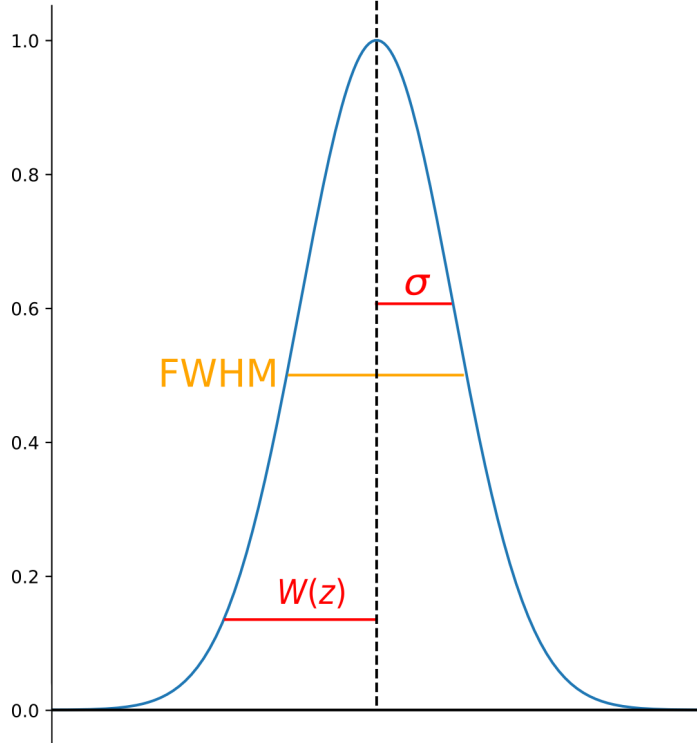


Figure 2.4.1: Normalized Gaussian profile. Different ways of measuring the width of the profile are displayed geometrically.

varying, this means that the envelope of the wave is approximately constant on a length of λ and we can write the complex electric field as $U(r) = A(r)e^{-ikz}$. If we can consider a wave propagating in the z direction, we can find a solution in the form of [35]:

$$U(r) = A_0 \frac{W_0}{W(z)} \exp \left\{ -\frac{x^2 + y^2}{W^2(z)} \right\} \exp \left\{ -ikz - ik \frac{x^2 + y^2}{2R(z)} + i \arctan(z/z_0) \right\}. \quad (2.4.1)$$

These solutions are called Gaussian beams, they are characterized by an amplitude A , a width $W(z)$, Rayleigh range z_0 , and a curvature radius $R(z)$. Let us take a look at the features that arise from these beams. The optical power can be calculate by taking the square of the complex amplitude

$$I(r) = |U(r)|^2 = I_0 \left(\frac{W_0}{W(z)} \right)^2 \exp \left\{ \frac{2x^2 + 2y^2}{W^2(z)} \right\} \quad I_0 = |A_0|^2. \quad (2.4.2)$$

It is clear from here why the beam is called Gaussian. For a fixed z , the beam shape is the one of a two dimensional beam profile, i.e. the sections in the $x - y$ plane of a Gaussian beams are Gaussian shaped distribution. If we further take a cross section in the $x - y$ plane, we end up with a one dimensional Gaussian distribution. This shape is shown in figure 2.4.1, along with some important parameters. It is important to understand how to characterize the width of a Gaussian shape, as it provides a quantitative way of measuring a laser beam width and its focus spot. A common way to define the width of a Gaussian distribution is according to the standard deviation σ , in this case the shape is given by $Ae^{-\frac{x^2}{2\sigma^2}}$, but for the intensity of a Gaussian beam, $W(z)$ is a much more used value. $W(z)$ is defined as the point at which the irradiance I has fallen to $1/e^2 = 13.5\%$

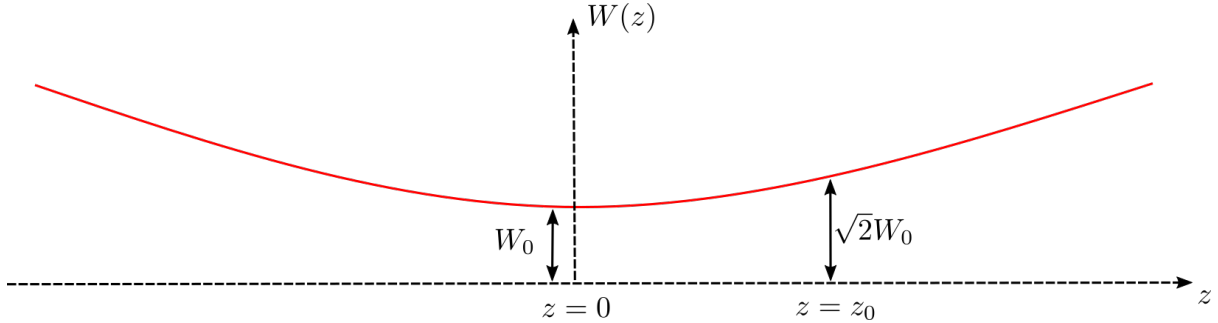


Figure 2.4.2: Width profile of a Gaussian beam. The beam is focused at the position z_0 , here it assumes the minimum width W_0 , also referred to as waist.

of its maximum value. The relationship between these two quantities is easily found: $W(z) = 2\sigma$.

Another common parameter to characterize the width of a Gaussian is the full width half maximum (FWHM), this can be found to be related to W as: $W = 0.84 \cdot \text{FWHM}$. All these methods are equivalent and are different only from a prefactor, so for the rest of the section, we can stick to $W(z)$ and study its behaviour. Always from Helmholtz equation [35], the profile of $W(z)$ is found to be

$$W(z) = W_0 \sqrt{1 + \left(\frac{z}{z_0}\right)^2} \quad W_0 = \sqrt{\frac{\lambda z_0}{\pi}}. \quad (2.4.3)$$

This equation is plotted in figure (2.4.2). There are several important features that can be seen. First of all, the width reaches a minimum in $z = 0$ at a value of W_0 , this is called focus of the beam and its width is the waist of the beam. Before and after the focus, the beam profile diverges almost linearly with an angle given by $\theta = W_0/z_0$, which means the smaller the focus, the greater it diverges. This property will become important later in the work, because it provides one limit on the focus spot. In fact, the optical aperture of the trap is limited by the electrodes, and a too diverging beam can potentially clip on one electrode causing aberrations and scattered light in the whole trap. The Rayleigh range z_0 also has a geometrical interpretation, it represents the point where the beam width is exactly $\sqrt{2}W_0$, along with θ this is a useful way to characterize how fast a beam diverges.

In real experiments, all of these beam quantities can be manipulated with a lens. A Gaussian beam can therefore be shaped at will using optical elements. In order to study such reshaping, let us consider a thin spherical lens with focal length f , and radius of curvature R_l placed at position z . The effect of the lens on the beam is to give an extra phase factor to equation (2.4.1) equals to $k(x^2 + y^2)/2f$ [36]. We can match the phase of the incoming and emerging waves

$$kz + k\frac{x^2 + y^2}{2R} - \zeta - k\frac{x^2 + y^2}{2f} = kz + k\frac{x^2 + y^2}{2R'} - \zeta \implies \frac{1}{R'} = \frac{1}{R} - \frac{1}{f}. \quad (2.4.4)$$

The effect of the lens is now clear, it changes the radius of curvature to R' according to the previous equation. Moreover, the width of the beam at the lens is not altered $W = W'$. Using these last two facts, we can determine all the parameters of the outgoing wave. The

most important for us is the new waist W'_0

$$W'_0 = MW_0 \quad M = \frac{M_r}{\sqrt{q + r^2}} \quad M_r = \left| \frac{f}{z - f} \right| \quad r = \frac{z_0}{z - f}. \quad (2.4.5)$$

M is the magnification factor which provides an easy way to describe the change of the beam. For a better understanding of this last result, let us consider an less general example. We can place the lens at the focus $z = 0$, and have a collimated beam $z_0 \rightarrow +\infty$. In this case the new waist is

$$W'_0 = \frac{W_0}{\sqrt{1 + (z_0/f)^2}} \simeq W_0 \frac{f}{z_0} = \frac{\lambda f}{\pi W_0} \quad (2.4.6)$$

where the approximation comes from taking $z_0 \gg f$. There are three parameters we can act on to achieve the smallest focus spot. The wavelength λ , the shorter the better. The focal length of the lens f must be as small as possible, and the waist of the incoming beam W_0 as big as possible. Usually the wavelength is fixed in an optical system, so the best way to achieve a small focus is to collimate the beam as large as possible, the limit is given by the diameter D of the lens. Hence, in the best case we have $D = 2W_0$ which means the waist is

$$W_0 = \frac{2\lambda}{\pi} \frac{f}{D}. \quad (2.4.7)$$

A system focused to this limit is said to be diffraction limited. Indeed, if the size of the collimated beam is yet increased, the lens becomes a finite size aperture and diffraction effects will appear at the image plane.

2.4.2 Beam steering via AOD's

Acousto-optical deflectors are a common practical devices to steer a laser beam. Their working principle is based on the Acousto-optical effect. A crystal is strained due to a acoustic wave. A piezo is used to create vibrations that propagate in the crystal, and it is absorbed on the opposite facet of the crystal. Vibrations compress and stretch the medium creating a pattern. Due to the different density of the crystal medium at different position, the refractive index is modified creating a grating that can be used to deflects light.

As a simple model, let us consider a rectangular crystal like in figure 2.4.3. The acoustic wave creates a sinusoidal pattern with frequency Ω_s and wavevector q , for the refractive index $n(x, t)$

$$n(x, t) = n - \Delta n_0 \cos(\Omega_s t - qx), \quad (2.4.8)$$

where n is the refractive index of the unperturbed medium, Δn_0 is the amplitude of the perturbation. Δn_0 is proportional to the square root of the sound intensity.

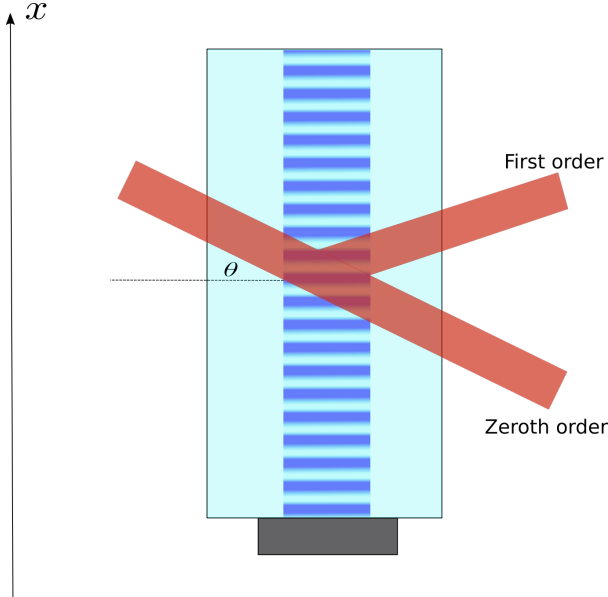


Figure 2.4.3: AOD.

The reflected wave can be calculated by dividing the crystal in thin layers, each with his refractive index $n(x)$. The total reflection is given by all the contributions $\frac{dr}{dx}$ of every layer, we can therefore integrate over a length L as follow:

$$r = \int_{L/2}^{L/2} e^{i2kx \sin \theta} \frac{dr}{dx} dx \quad (2.4.9)$$

The included phase takes into consideration the different phase of the input beam when different layers are met. The integral can be solved with a change of variable

$$\frac{dr}{dx} = \frac{dr}{dn} \frac{dn}{dx} = \frac{dr}{dn} q \Delta n_0 \sin(\Omega_s t - qx), \quad (2.4.10)$$

The sine function can be written as exponential and now the integral contains only exponential functions which are trivial to calculate. At the end we obtain two contributes for the reflected wave r :

$$r = r_+ + r_- \quad r_{\pm} = \pm i r_0 \text{sinc} \left[(2k \sin \theta \mp q) \frac{L}{2\pi} \right] e^{\pm i \Omega_s t} \quad (2.4.11)$$

These two terms are the plus and minus first order diffraction, an acousto-optical device can be operated symmetrically entering either with a positive angle or with a negative one. Since the maths and the physics is the same, we will focus only on the positive term, called upshifted Bragg diffraction. The sinc function peaks sharply when its argument is 0, i.e. at $2k \sin \theta = q$, and then quickly decreases as the angle is changed. Hence, the input beam must enter with a particular angle in order to diffract. The condition to be satisfied is usually called Bragg condition, and can be written as a function of the wavelengths as

$$\sin \theta = \frac{\lambda}{2\Lambda_s} \quad \Lambda_s = \frac{2\pi}{q}. \quad (2.4.12)$$

If the condition is not perfectly matched, some light will not be diffracted and will be

transmitted unaltered through the device. The ratio of the transmitted and diffracted light is called diffraction efficiency and gives an idea of how well an acousto-optical device is performing.

From equation (2.4.11) we can notice that an extra phase factor proportional to $\Omega_s t$ is added to the reflected wave. Thus, if the incoming wave is oscillating at $\propto e^{i\omega t}$, the diffracted wave will oscillate as $\propto r_+ e^{i\omega t} \implies \propto e^{i(\omega + \Omega_s)t}$. The frequency of the diffracted wave ω_r is therefore shifted by the frequency of the acoustic vibration as

$$\omega_r = \omega + \Omega_s. \quad (2.4.13)$$

This fact already suggests an application for acousto devices: they can be used as tuning device to shift the frequency of a laser. This kind of devices are called acousto-optical modulator (AOM). However, it is not the only application, we can also use the same device to deflect a beam. The idea is to change the deflection angle θ by changing the frequency Ω_s applied to the crystal. Assume that the angle θ is small enough to approximate $\sin \theta \sim \theta$, the Bragg condition can be written as

$$\theta \simeq \frac{\lambda}{2v_s} f, \quad (2.4.14)$$

where v_s is the speed of sound and f the frequency of the signal. We can already see that if we change the frequency f , the deflection angle θ changes proportionally. Although the Bragg condition (2.4.12) is not satisfied anymore, we can work with small enough angles that the diffraction efficiency remain above a certain thresholds. The bandwidth is defined as the possible scanning angles, if B is the frequency bandwidth in which the diffraction efficiency stay above a certain number (50% for instance). Then, the range of scannability is

$$\Delta\theta = \frac{\lambda B}{2v_s} \quad (2.4.15)$$

there are several ways to engineer such device to increase bandwidth and keep the Bragg condition verified, for example the transducer is replaced by a phase array of transducers that tilt the acoustic beam [37].

2.5 Experiments model

2.5.1 Addressed photon generation

2.5.2 Addressed qubit manipulation

Ions can be used as sensitive tools for beam profiling, unfortunately the 393 nm light excites a dipole transition with a short lived excited state. Therefore, a direct excitation followed by a measurement is not fast enough to gain any information. Ideally, the 729nm qubit transition should be used, as here state readout is available and the transition is metastable. This is possible as the 393nm transition shares the ground state with the qubit transition, so the 393nm laser can be detuned such that the AC Stark shift caused changes the phase of the qubit producing measurable effects. Measurements of the Stark shift can be done with a Ramsey interference experiment [16]. The idea of the experiment is to send a resonant $\pi/2$ pulse at 729nm, which bring the qubit state to a superposition



Figure 2.5.1: Experiment sequence

$|S\rangle + |D\rangle$, here another in phase resonant $\pi/2$ pulse at 729nm would bring the final state to the excited level $|D\rangle$. However, if between the two 729nm pulses, AC stark shift is induced by a pulse of 393nm light, an additional phase is added to the superposition $|S\rangle + |D\rangle$, and the final state after the second 729nm pulse will depend on the shift induced by the 393nm laser. By calculating the final probability P_D it is possible to infer the power of the 393nm light. Rigorous mathematic can be done with matrices (2.1.17) here called U_{729} and (2.1.22), referred to as U_{393} . After the three pulse sequence the final state is

$$\begin{aligned} |\psi_f\rangle &= U_{729}(\pi, \phi) U_{393}(\delta) U_{729}(\pi, 0) |S\rangle \\ &= \frac{1}{2} \left(e^{-i\frac{\delta}{2}t} - e^{-i\phi} \right) |S\rangle - \frac{i}{2} \left(1 + e^{-i\frac{\delta}{2}t} e^{-i\phi} \right) |D\rangle \end{aligned} \quad (2.5.1)$$

where $\delta = \Omega^2/4\Delta$ is the Stark shift, and Ω is the Rabi frequency of the 393nm light that we want to measure. The final probability is then

$$P_D = \cos^2 \left(2\phi + 2\frac{\delta t}{2} \right) = \cos^2 \left(2\phi + \frac{\Omega^2 t}{4\Delta} \right). \quad (2.5.2)$$

As we can see, the final signal depends on the phase of the second 729nm pulse ϕ and on the Stark shift induced by the 393nm laser. To get Ω^2 a simple formula inversion can be done $\Omega^2 = [\arccos(\sqrt{P_D}) - 2\phi]$. The phase ϕ can be chosen freely and all constants have been dropped as the data will be normalized.

The experiment sequence is in figure 2.5.1, for every sequence, a stage of Doppler Cooling at the beginning is included, and at the end of the pulses PMT readout is performed. The sequence is then repeated N times to estimate the excitation probability for every data point. Between the Raman pulse and the second $\pi/2$ pulse, there is also a dead time which can be adjusted to improve signal to noise ratio.

The 393nm pulse has to be off resonance from the transition to avoid spontaneous scattering in the $S_{1/2} \rightarrow P_{1/2}$ transition. The detuning is therefore chosen such that the ratio of the Stark shift δ and the spontaneous scattering rate Γ_{eff} is at least 100. Using the value from table 3.1.1

$$\frac{\delta}{\Gamma_{eff}} = \frac{2\Delta}{\Gamma} \implies \Delta \sim 3 \text{ GHz}. \quad (2.5.3)$$

Chapter 3

Existing experimental system

The work developed in this thesis lies on top of an existing experiment. In this chapter we are going to describe the essential parts of the already existing setup on top of which the addressing system has been build. Calcium-40 ions are used in the experiment, the implementation of several techniques for trapping and manipulating these ions are discussed. Furthermore, the addressing setup utilizes 393 nm light, the laser emitting this light was already installed and used, thus that setup is presented. The experiment can be controlled remotely via computers, an overview of how it is implemented and how it works is also given.

3.1 Ion trap and key techniques

3.1.1 Calcium Ions

In choosing the appropriate ion to trap, one looks first of all for simplicity, which means choosing an element with one single electron in the most outer orbital. This fact limits the choice to the second group of the periodic table, many of these elements have been successfully trapped: beryllium [38], barium [39], strontium [40], and calcium [41]. The latter has been chosen for this experiment, as calcium has transitions easily accessible with commercial diode and titanium-sapphire lasers. The most abundant isotope of calcium is calcium-40, which is a common choice, but not the only one [42]. Nevertheless, $^{40}\text{Ca}^+$ ions were our choice. In figure 3.1.1 the level scheme of the only electron in the outer shell is presented. A single ground state is present $S_{1/2}$ with no hyperfine structure as $^{40}\text{Ca}^+$ does not possess a nuclear spin. There are two short lived excited states (~ 7 ns): $P_{1/2}$, and $P_{3/2}$ which are accessible with dipole transitions. These states have different decay channels, for $P_{1/2}$ the branching ratios are 6% to $D_{3/2}$, and 94% back to the ground state. For $P_{3/2}$ there is a probability of 5.3% to decay to $D_{5/2}$, 0.6% to go to $D_{3/2}$ and 94% to return to $S_{1/2}$. Due to the short lifetimes of these two states, they are suitable for laser cooling and state detection, while the states $D_{3/2}$ and $D_{5/2}$ are metastable (~ 1 s) since accessible with electric quadrupole transition. Since the lifetime of the D states are much greater than typical coherence time, they can encode a stable qubit and manipulated without worrying about dissipative process. Table 3.1.1 summarizes details about the different transitions, and what they are used for. A more detailed description and implementation is discussed in the next section.

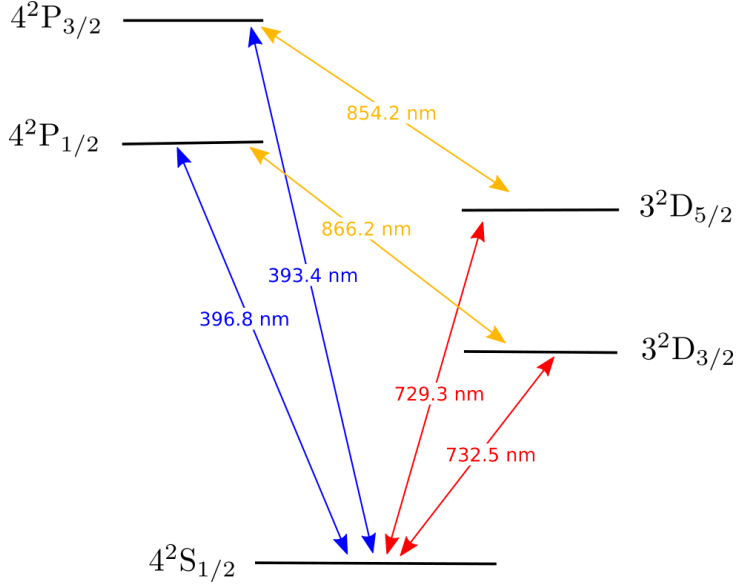


Figure 3.1.1: Level scheme of $^{40}\text{Ca}^+$ with main transitions highlighted. Blue transitions are dipole transitions suitable for cooling, imaging and photon detection. Red transitions are dipole forbidden, but accessible with electric quadrupole, they are used to encode qubits. Orange transition are usually repumped. In addition, the 854 nm transition is tuned in resonance with the cavity for photon generation purposes. From more and precise value see table 3.1.1

Transition	wavelength (nm)	Decay rate Γ	Lifetime τ	Main use
$S_{1/2} \rightarrow P_{1/2}$	396.847	$2\pi \times 20.8$ MHz	7.7 ns	Cooling and imaging
$S_{1/2} \rightarrow P_{3/2}$	393.366	$2\pi \times 21.4$ MHz	7.4 ns	Photon generation
$S_{1/2} \rightarrow D_{3/2}$	732.389	$2\pi \times 0.132$ Hz	1.080 s	-
$S_{1/2} \rightarrow D_{5/2}$	729.147	$2\pi \times 0.136$ Hz	1.045 s	Qubit
$P_{1/2} \rightarrow D_{3/2}$	866.214	$2\pi \times 1.70$ MHz	94.3 ns	Repumping
$P_{3/2} \rightarrow D_{5/2}$	854.209	$2\pi \times 1.34$ MHz	101 ns	Cavity photon
$P_{3/2} \rightarrow D_{3/2}$	849.802	$2\pi \times 1.52$ MHz	902 ns	Repumping

Table 3.1.1: Transitions in $^{40}\text{Ca}^+$ and current use in the experiment. Values are taken from [33, 43]

– Add lasers direction!

3.1.2 Trapping, cooling, and state readout

Our trap is a linear 3D RF Paul trap as depicted in figure (), the picture of the real trap is displayed in figure 3.1.2. The trap consists of 4 orthogonal electrodes with blade shape for RF confinement in the radial direction. In the axial direction confinement is achieved with two tip electrodes that forms the endcaps. Everything is made in titanium, it is covered in gold and the trap itself is mounted vertically on a Shappire holder. The endcaps are 5 mm apart, and they are usually kept at a voltage in the order of 500-1000V, which means an axial frequency of $\omega_z \sim 2\pi \times 0.7 - 1$ MHz. The four blades are 0.8 mm from the center

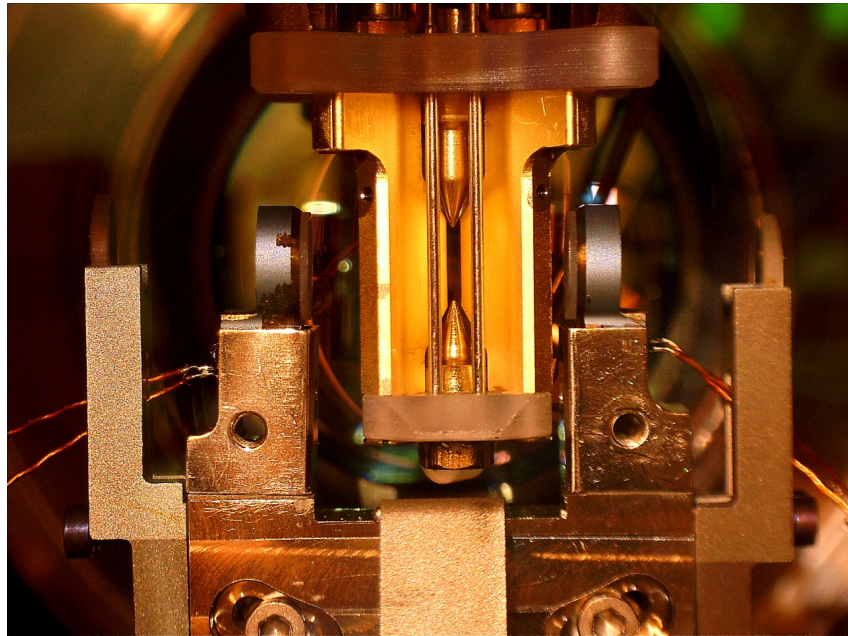


Figure 3.1.2: Photo of the mounted trap, a pair of compensation electrodes and the mirrors of the cavity are also visible.

of the trap and driven with an RF of ~ 24 MHz. Due to the high power delivered to this blades (~ -4 dBm), the RF signal has to be impedance matched with the trap, this is done with an helical resonator. The trap also includes three pairs of compensations electrodes that can be used to compensate micromotion. Loading of ions is done with an atomic oven, calcium is heated and directed towards the trap, in the trap the atoms undergo 2-stage photon ionization. The first laser 422 nm, excite one electron to a very high excited state, the second laser 375 nm, brings the electron to free space ionizing the atom. Such two stage process allows to filter for isotopes and ionize only ^{40}Ca . Loading usually takes minutes or tens of minutes depending on the number of ions one wants to load. Storing time can be in the order of days, especially when a single ion is loaded. Once loaded, ions are laser cooled with 397 nm light on the transition $S_{1/2} \rightarrow P_{1/2}$ detuned at $-\Gamma/2$. An additional repumper on the transition $P_{1/2} \rightarrow D_{3/2}$ is also used to avoid for the electron being stuck in the $D_{3/2}$ state. For typical experiment a stage of doppler cooling is always included, this lasts from 1 millisecond up to tens of milliseconds. With the same Doppler cooling light, imaging can also be done. The light shines on the ions exciting the transition $S_{1/2} \rightarrow P_{1/2}$ driving the electron to the excited states which then decay spontaneously emitting a photons. Photon are collected with a custom objective with NA of ~ 0.3 , which means an efficiency of 2.5 % over the solid angle 4π . The objective focuses the collected photons 1.5 meters away where a CCD camera (Andor iXon Ultra 897) is placed. The geometrical path of the imaging is displayed in figure 3.1.3, this setup has a magnification factor of ~ 18.6 . The same objective is also used for the addressing setup built within this thesis. Therefore, the imaging optical path must be partially shared with the newly built addressing. In depth overview of objective is therefore given in section 4.2.

State read out is possible with this kind of imaging, with the difference of using a photomultiplier tube (PMT) for counting photons instead of a camera. Consider a qubit encoded in the states $S_{1/2} \rightarrow D_{5/2}$, if the imaging laser is switched on, the electron will be projected either to the $S_{1/2}$ level or in the $D_{5/2}$. In the first case, photons are scattered

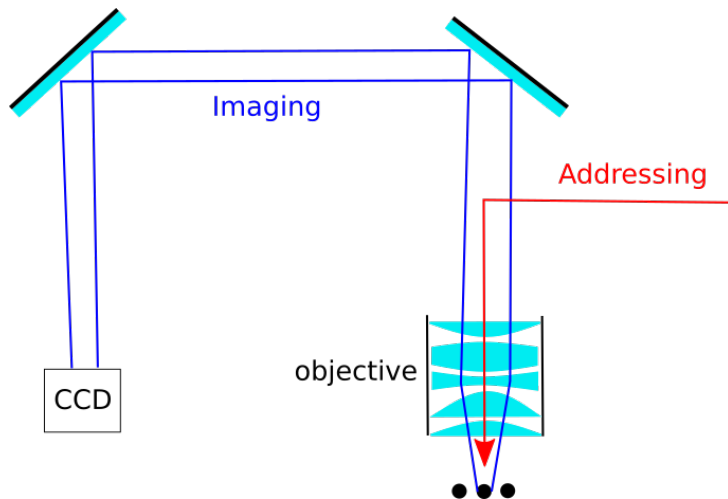


Figure 3.1.3: Top view of the imaging optical path, the objective collimates and focuses the scatter photons onto the CCD camera. The addressing setup must share part of this path, as the same objective is used for focusing.

from the ion and collected on the PMT, in the second case the electron is shelved and will not scatter any photon. Hence, the two cases are distinguishable by counting statistics. An histogram can be constructed with the number of photon measured, and a properly set threshold differentiates between bright and dark states. Typical detection times are in the order of milliseconds.

3.2 393 nm laser

The laser used to drive the Raman transition is 393 nm. This light is obtained from a titanium-sapphire laser from MSquared. The laser is optically pumped with 8 W of light at 532 nm coming from a Lighthouse Photonics Sprout laser. The active Ti:Sa crystal is contained in a cavity in a bow tie configuration, together with an optical diode, etalon, birefringent mirror, and tunable cavity mirror for frequency tuning and stabilization. The fundamental mode is at 786 nm with tunability ranging from 725 nm to 875 nm that can be controlled remotely on the computer. The laser can also be locked to a wavemeter and tuned with it. The fundamental light is frequency doubled to 393 nm via a MSquared ECD-X external cavity resonant doubler accessory module. Blue light can be obtained with up to 1 W of power. Before reaching the ion trap, 393 nm light is sent through the setup in figure 3.2.1. There are two AOM's in the setup, AOM1 from Brimrose with a working frequency of 150 MHz, AOM2 is still from Brimrose and works at 80 MHz. There are two paths for the light: a resonant one which gets resonant light from the laser, and send it directly to the ion. This path is the zeroth order of AOM1, light is not diffracted, but it is coupled to a fiber using a PBS, and then goes to the ion trap. The second path is the detuned one, the main purpose is to red detune the laser light in order to excite the Raman transition. This path goes through both AOM's, the first AOM1 is in double pass configuration and shift the light by 300 MHz. Diffracted light in the -1 order is sent through and reflected back again in the same AOM by a prism. Diffracted light from AOM1 is sent to the second AOM used in single pass configuration which further shift the light by 80 MHz. The diffracted light (-1 order), from AOM2, is coupled to a fiber

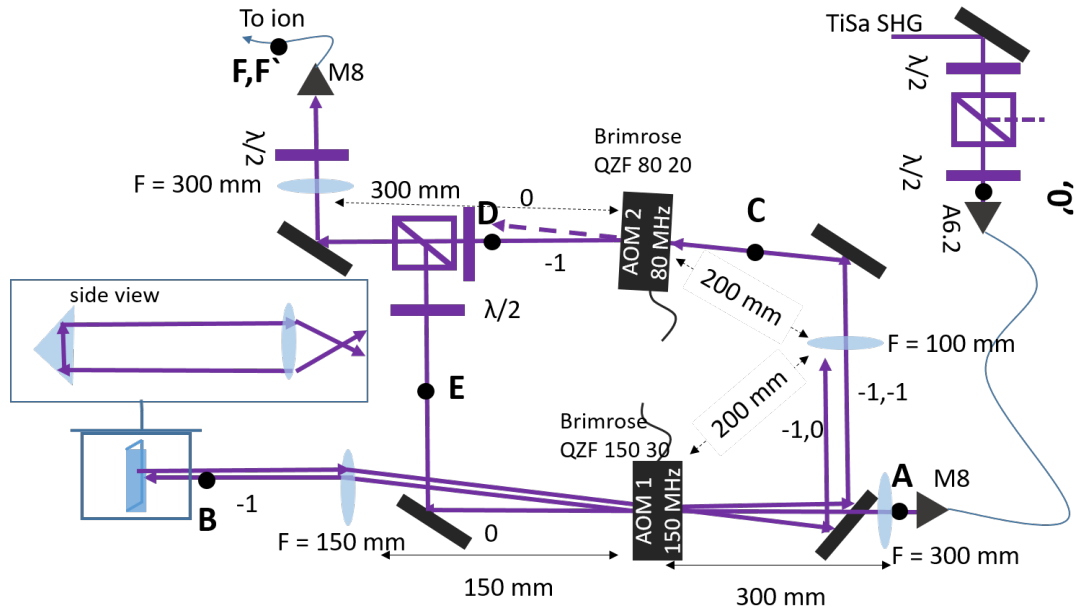


Figure 3.2.1: 393nm laser optical setup. Two paths are present, a resonant one, and a detuned that goes through two AOM's.

that brings it to the ion trap. The detuned beam therefore reaches the ion with a -380 MHz detuning which can be modulated within the bandwidths of both AOM's. The zeroth order of AOM2 is blocked to avoid that this light is coupled to the fiber and end in the trap. Lenses in the setup have the purpose to focus the waist of the beam in the AOM's aperture avoiding unwanted beam steering and therefore losing coupling to the fiber. AOM2 is also used to generate a bichromatic field, simply by driving this AOM with a multifrequency signal.

This particular setup had to be altered after the installation of the addressing setup, minor adjustment had to be made in order to compensate for an additional frequency shift due to the AOD in the addressing setup. AOM2 was switched from -1 order to +1 order, and driving frequency were changed to 180 MHz for AOM1 and 70 MHz for AOM2.

3.3 Experiment control

Complex experiments require control over a large network of AOM's and other devices. Furthermore, laser pulse coherence is also fundamental in some sequential experiment. The need of fast and coherent pulse control is fulfilled by an electronic system that can be controlled with a software on a computer where every device connected to the network can be controlled. The experiment control network is sketched in figure 3.3.1. On the computer TrICS software is installed, this computer is connected to a BUS system with a NIDAQ card. Direct Digital Synthesizers (DDS) used to generate radio frequency signal for AOM's are connected to the BUS system through an optocoupler to avoid ground loops. Therefore, the computer can send electric signal over the BUS to specific DDS allowing for direct control. The computer is also connected via ethernet to a Pulse Box, and through another NIDAQ card to the same box. The card sends and receive trigger signals, while over the ethernet, sequences are uploaded. The pulse box contains DDS and FPGA, thus it has the capabilities of generating short and coherent TTL pulses

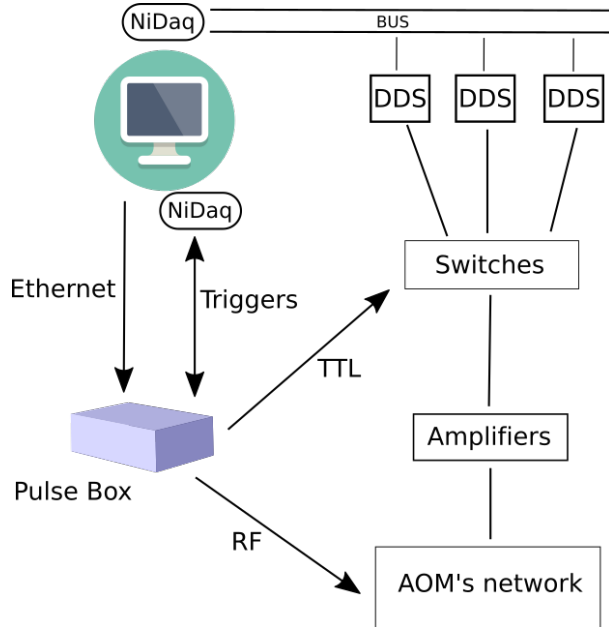


Figure 3.3.1: Schematic of the experimental control. Everything is controlled remotely by a pc. During a sequence a pulse box generated coherent pulses to the appropriate devices.

(μ s) that can send to TTL switches placed between a DDS, the source of the signal, and an AOM. The Pulse Box contains fast switching DDS, this means that the frequency of such DDS can be changed quickly, unlike the DDS on the BUS. The whole system runs with two separated clocks, one at 10 MHz, and another one at 1.2 GHz.

With this system, a laser pulse can be controlled in frequency, amplitude, and length. Frequency and amplitude are set in the DDS by sending a signal over the BUS system to the appropriate DDS channel. The length of the pulse can be controlled precisely by the Pulse Box. Moreover, the Pulse Box also has pulse shaping possibilities.

In a typical experiment, a sequence of pulses is programmed in python on the computer. When the experiment is run, the computer uploads the sequence to the FPGA inside the Pulse Box. Next, the computer updates the DDS on the BUS with the appropriate values for the experiment, sends a trigger signal to the Pulse Box and the Pulse Box generates and sends all the signals for the sequence. When the experiment is done, the Pulse box sends another trigger back to the computer, which proceeds to prepare for the next measurement point, it updates the values of the BUS DDS, reupload the code to the Pulse Box, sends a trigger to start the sequence and the loop is repeated.



Figure 3.3.2: Trics software used to change all the experiment parameters and launch measurements.

Chapter 4

Design and simulation of the addressing setup

The purpose of this thesis work was to design and build the addressing setup for the already existing experiment. In this chapter we discuss the design and the implementation of such setup. The design is a crucial part of the work, there are several requirements that have to be met in order to achieve the proper needed functionality. In the first section, the requirements are presented together with an overview of the design idea. In the setup an objective was already present, and the choice of an AOD was already made. Hence, we discuss this components as given. The rest of the setup was simulated with the software Zemax, which was used to find the optimal optical components and their placement.

4.1 Addressing system overview and requirements

Addressing systems have already been developed and employed in experiments successfully. Different techniques are available: the main idea is to focus a laser beam tighter than ion-ion separation and steer it. In Innsbruck calcium ions have been addressed in this way, where the steering was achieved with an AOD [44]; Beam has also been steered with micro-electromechanical systems (MEMS) mirrors [45]. Another idea is to send a normal beam illuminating all the ions, but hiding those who are not addressed. This was done with Ytterbium atoms where by means of a inhomogeneous magnetic field the transition frequencies were shifted shielding selected ions [46].

Our choice was to implement the already successful idea of Innsbruck with an AOD and improve it. The advantage of AODs is to have a fast switching time in the order of μs , that is used for fast switching between ions. A problem with the implementation of [44] is however the fact that the AOD is placed right before the beam expander, this limits the addressing range, as the beam is likely to clip when it is steered on the edge of the AOD's bandwidth. This is the main problem that the new designed system, here implemented, wanted to address: exploiting the full capabilities of the AOD while maintaining a very tight focus. Therefore, there are mainly two aspects to keep in mind, the focus spot and the addressing range. However the priority was the focus spot as a large addressing range is not essential.

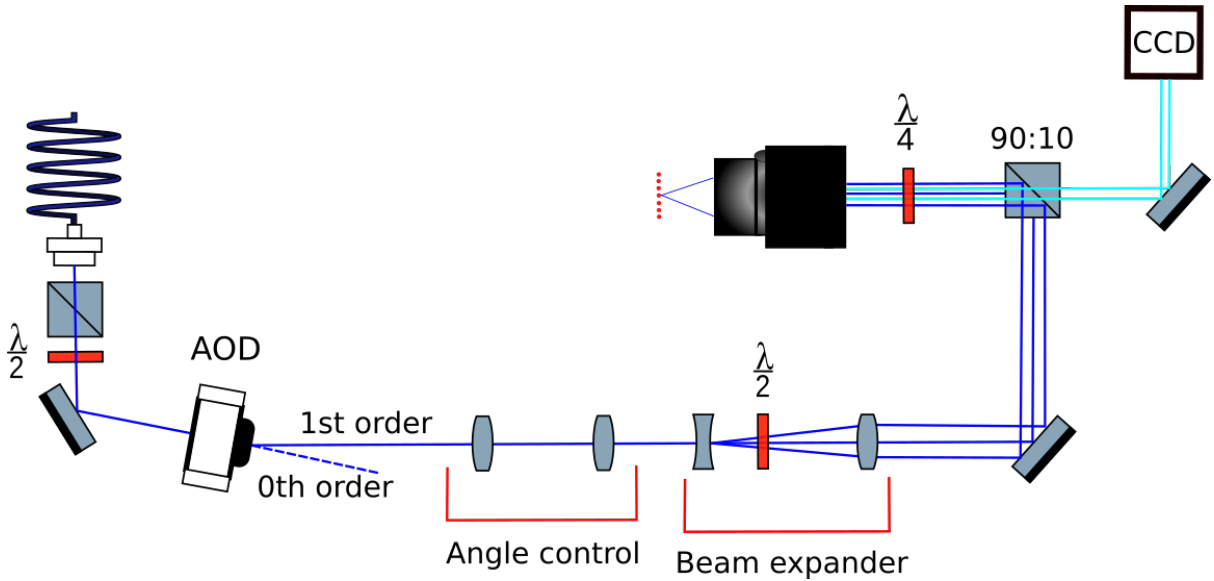
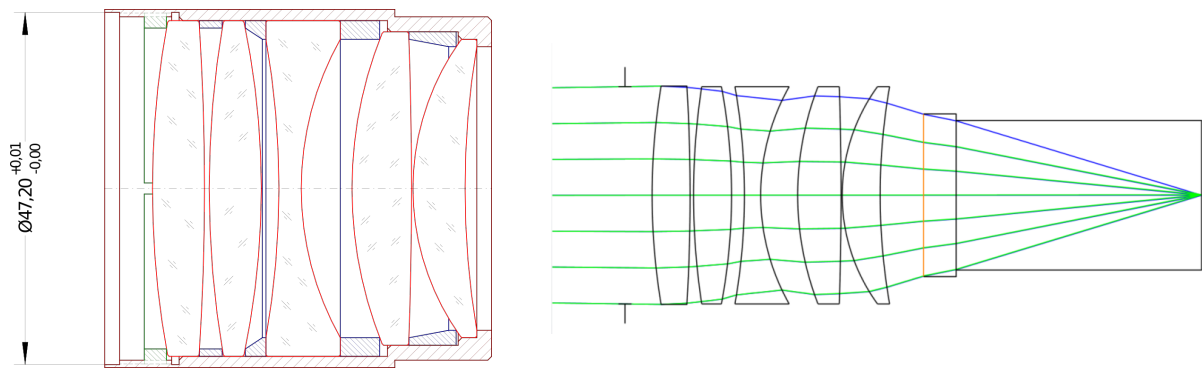


Figure 4.1.1: Scheme of the setup. Light comes from a fiber, polarization is cleaned, and then sent thorough the AOD. 1st order diffracted light is refocused into a beam expander, where the beam is broadened before being focus by the objective. Light blue lines represents 393 nm light coming from the ions into the imaging setup.

The addressing setup should be able to address single ions in a string in order to generate single photons out of single ions via the already discussed Raman process. Ion separations, in the case of $^{40}\text{Ca}^+$, has been derived in section 2.3.2, for a trap frequency of 1 MHz is $5.6 \mu\text{m}$. The setup must therefore be able to focus tightly a laser beam down to 1-2 μm . As seen in section 2.4.1, a tighter focus can obtained with a shorter wavelength, a bigger lens, or with shorter focal length. The focusing lens, a.k.a the objective, is shared with the imaging setup, and thus it is given, the focal length is therefore a constant in the problem. The wavelength is also a constant, as the Raman process happens only at 393 nm. This gives only one possibility left to tighten the focus, i.e. by making the beam as broad as possible at the objective input surface. Beam expansion can be achieved with a Galilean telescope, it take two lenses to form such Telescope, a concave Lenses to diverge a collimated beam and a convex lens to collimate the diverging beam. The combinations of these two lenses takes a collimated beam and expands it to another collimated beam. This expansion part is one of the two essential part of the addressing setup. The other part is related to addressing range. Not only, we want to focus the beam to a single ion, but we want to move the beam as well, such that it focuses on a different ion. Therefore, there is a requirement also on the range that can be addressed. This depends on the number of ions and their spacing, a good aim is to address tens of ions, this requires the ability to move the focus in one direction by $150\text{-}200 \mu\text{m}$. Beam steering is possible with the use of an AOD, the detailed working principle of this device has been discussed in section 2.4.2. Basically the angle of the output beam of the AOD changes as the driving frequency changes. However, the AOD must be placed far behind the objective to leave space for the beam expander, this implies a need to control and redirect the angle of the AOD's output beam to send it to the beam expander and later in the objective without any clipping. This task is accomplished with a pair of converging lenses, they refocus the collimated beam into the beam expander, beam then becomes wider, reaches the objective and it is focused on the ion. It is important to get the right lenses at the right distances,

the objective has 5 different lenses inside and it works slightly differently from a normal lens. For instance, it does not focus collimated blue light, but red. This means that the beam expander should not collimate completely the beam but rather expand it and leave it diverging, so that the objective can focus it at the right position. The setup displayed in figure 4.1.1 also contains polarization optics. As discussed in section 2.2.3, Zeeman transitions are polarization sensitive, thus polarization control is required. The AOD is polarization sensitive, which means it requires a certain input polarization and outputs another particular polarization, that is the reason why half wave plate are before and after, and additional quarter wave plate is inserted before the objective to obtain circular polarized light. This placements means having a bigger plate than standard, but if placed before in the optical path, the mirror and the beam splitter could alter the polarization. Moreover, the quarter wave plate is zeroth order and custom made, in order to have a greater polarization stability. The choice of using a beam splitter is also peculiar, to separate light at different wavelength it is common choice to use a dichroic mirror, however the light in the imaging path is 397 nm, very close to the 393 nm light of the addressing setup. This would have meant using a very narrow dichroic, the alternative was to use a 90:10 beam splitter, where 90 % of the light is transmitted and only 10 % of the light is reflected. The addressing therefore loses 90 % of the power on this splitter, but that is not a problem, since it is always possible to get more light out of the laser. Furthermore, this light is focused so tightly that even a small amount of light can excite the ions. On the other end, it is not really possible to get more scattered light from the ions, so 397 nm light and the imaging setup must be as efficient as possible, with 10 % of losses, ions are still visible on the camera and on the PMT.

4.2 Objective and AOD



(a) Section of the custom objective, red parts are the lenses, while the rest is the housing.

(b) Zemax simulation of the objective. On the right, viewport and the vacuum chamber are also present.

Figure 4.2.1

The objective used to focus the light was already present in the system and had to be taken as it is. It is a custom objective by Sill optics placed outside vacuum, the section is in figure 4.2.1a. It contains 5 lenses inside a mechanical housing, the aperture is about 47 mm large in diameter. This objective has different purposes, it was designed keeping in mind: imaging of ions, addressing with red light and addressing of blue light. The objective has

to perform all three of this jobs fairly well, which means it has light transmission $>90\%$, every lenses is AR coated, numerical aperture of $NA = 0.3$. Moreover, it is telecentric, which means that the focus spot should move perpendicularly to the optical axis if the beam is steered. Lastly it was also designed to take into consideration the fact that it is placed out of vacuum, the light after the objective has to go through a 6 mm fused silica viewport before entering the vacuum and after further 40 mm encounters the ions. The focal length of the objective is 54.07 mm at 729nm. The objective is also mounted on a 3 dimensional translational stage to allow for imaging and addressing calibration.

The AOD is from Gooch & Housego, model 4120-3. It has a specified central frequency of 120 MHz, with 50 MHz, bandwidth, so the driving frequency ranges from 95 to 145 MHz with a maximum RF power of 0.3 W. Therefore, the angle of deflection should be $\pm 0.86^\circ$. In this bandwidth the diffraction efficiency should remain above 75 % and have an average of 83 %. Further light is lost as much as 3% of due to insertion losses. The active aperture measures 3×3 mm, and the polarization has to be horizontal when entering the AOD, while it gets rotated during diffraction, as the specified output polarization is vertical.

4.3 Design simulation

The setup in figure 4.1.1 has been simulated with the software Zemax. The simulation had the purpose of assessing the performance of the setup, i.e. checking the viability of the setup and see if it meets all requirements. It was also used to find the best lenses for building the setup and the best placement. Not everything was simulated, bu only the essential parts. This includes the four lenses, the objective, the viewport and the vacuum chamber. As there is no option to simulate an AOD, it was not taken in consideration, instead the simulation started at the output of the AOD as described below. Mirrors and beam splitters also do not alter drastically the optical path and therefore there was no need to simulate them.



Figure 4.3.1: Zemax simulation of the setup. Rays propagate from left to right, only the four lenses are displayed, objective and image plane are far on the right. Different colors indicate different fields at different angle

The simulations start by specifying the input fields, these represent the physical light beam. To account for the different angled beams at the output of the AOD, three different fields has been simulated. One is along the optical axis, while the other two are angled corresponding to the extrema of the AOD bandwidth, so $\pm 0.86^\circ$. Therefore the propagation of these beams represents three different situations of beam direction and should also give an idea of the behavior in between the extrema. Next, the four lenses of the setup were inserted in Zemax, initially with variable radius and thickness. The Zemax file of the objective came from the company which designed it and was simply imported in the project. After the objective the 6mm viewport glass was included and

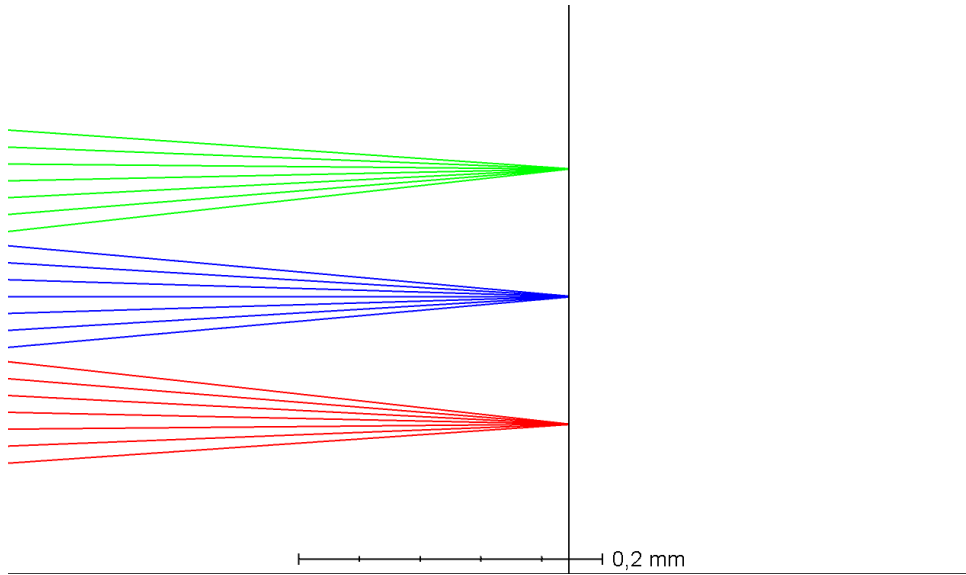


Figure 4.3.2: Zemax simulation at the image plane, where the ions are. The three colors are three different fields with different angles that are focuses at different position along the ion string. The full addressing range here displayed is about 168 μm .

then vacuum for 38.6 mm, which is the distance between the outer facet of the glass and the ion axis. The image plane was therefore set here. The distance between the last lens of the objective and the viewport was unknown, but a good estimation¹ allowed to progress with the simulation. The physical simulation in the software was carried out with the tool Physical Optics Propagation (POP). POP works by propagating a wavefront represented by an array of discrete points. The array is propagated through every optical component and free space. This method can be used to simulate coherent Gaussian beam with high precision as well as wave phenomena such as diffraction and aberrations. The initial value given to the propagator was the waist of the collimated beam out of the AOD. Since the beam going to the AOD comes from a fiber collimator, the value specified was taken from the datasheet of the fiber collimator, namely Scäfter + Kirchhoff 60FC-M12-33 [47]. Therefore, the specified waist was 1.08 mm.

The first step of the simulation work was to find the appropriate lens to build the setup. The thickness and the radius of the lenses was optimized trying to achieve the best focus spot while maintaining a good addressing range. Once obtained the desired situation, the lenses were found with the Zemax tool *Stock Lens Matching*. Basically the tool compares the simulated lenses with those in a catalogue from different companies and find the closest match. We opted to rely on the provider Thorlabs, so the search was limited to this company. Found lenses were in order from left to right LA-1059, LA-1131, LA-4252, and LA-1725 and can be seen in figure 4.3.1. Once the desired lenses were found, their Zemax files provided by the company were imported in the project and further optimization was carried on.

The second step was to optimize the lenses position always in view of finding the best focus spot while keeping a good addressing range. This was done using the optimising tools of Zemax and the merit function. The software can perform multivariate analysis

¹A posteriori, this assumption was not well suited and lead to some errors in the test setup. The correct value could be found by simulating the imaging setup and optimizing this distance to get the focus onto the camera.

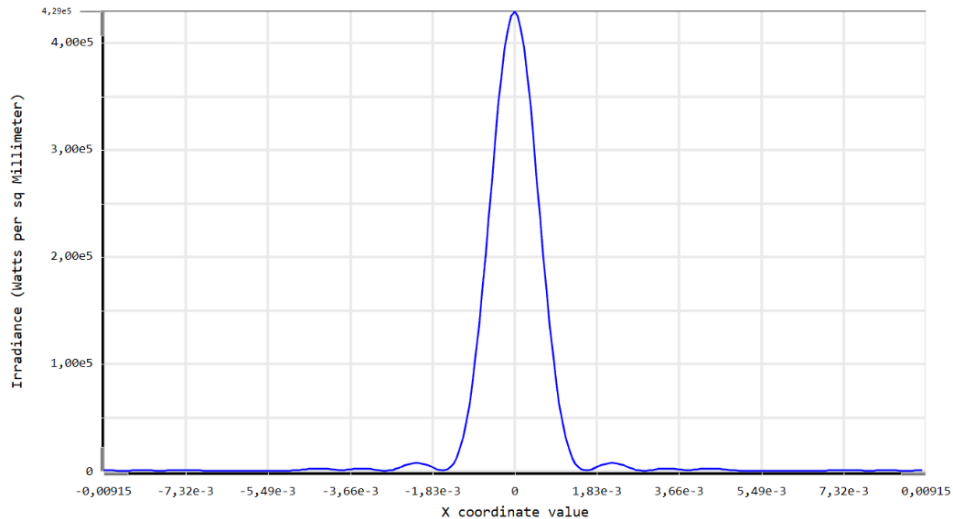


Figure 4.3.3: POP of the central field at the ion position, x cross section is displayed.

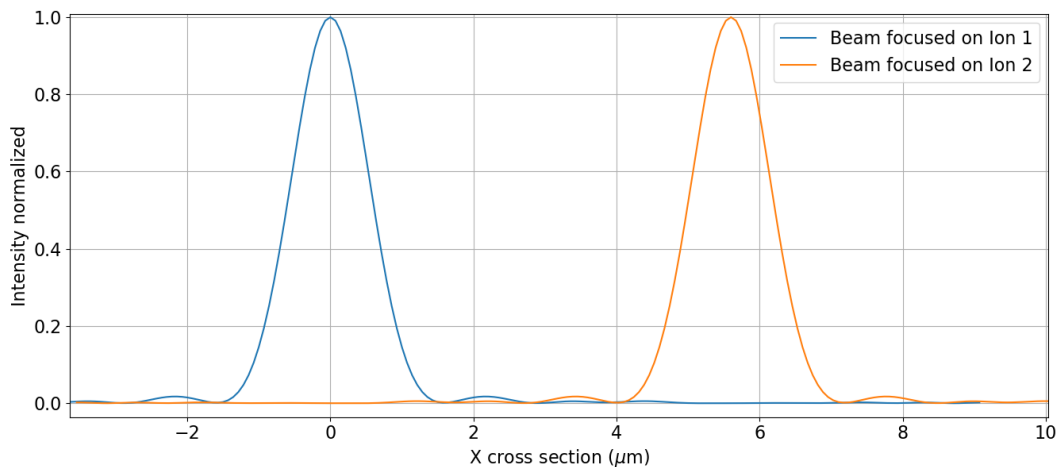


Figure 4.3.4: Beam focused at two different positions, where ions have their equilibrium position. From estimation of the addressing error can be made.

and minimize the focus spot depending on all the assigned variables, which in this case were the distance between the lenses. The final results can be seen in figure 4.3.3, the addressing range is 168 μm , while the waist is 1.02 μm .

Another important parameter for the performance of the setup is the addressing error. In the case of the beam focused on one ion, the addressing error is the leaking light on the neighbours ions. It can be a problem in the case of aberrations that produce bumps on the side of the main Gaussian peak. Especially in the case of diffraction limited system, the profile of the beam is a sinc function that can have more local maxima around the central peak. To estimate the addressing error, two ions are placed next to each other at 5.6 μm , and the respective addressing beam has been simulated. The intensity profile has been plotted in figure 4.3.4 and addressing error is calculated as $I_1(x_2)/I_1(x_1)$, where I_1 is the intensity profile of the beam focused on the left ion and x_1, x_2 are the positions of the two ions. From the simulations we get $I_1(x_2)/I_1(x_1) \simeq 10^{-4}$.

Another aspect that was simulated is the beam profile inside the trap. Optical access to the trap is limited and a tightly focus beam also has a large divergence, which could lead



Figure 4.3.5: Losses on the compensation electrodes as a function of the beam waist

to clipping on the trap's blades or compensation electrodes scattering light all around the trap and thus creating problems. In figure 4.3.6 the top view of the trap is plotted. The blue line represents the radius $W(z)$ from equation 2.4.3 of the addressing beam in the case of a waist W_0 of 1 μm . There is no apparent clipping, and the main problem seems to be the compensation electrodes. Since the beam is Gaussian, there is always a clipping part. To determine the fraction of power lost due to clipping on the compensation electrodes, we can calculate the transmitted power through the electrodes:

$$P_t = \int_{-\infty}^{\infty} dy \int_{-x_c/2}^{x_c/2} dx P(z), \quad (4.3.1)$$

where $P(z)$ is the power of the Gaussian beam, and x_c is the horizontal position of the compensation electrode. The integral can be computed numerically at position z of the electrodes. The result is plotted in figure 4.3.5, where the lost power $1 - P_t$ is plotted as a function of the waist W_0 .

4.4 Physical implementation

Once the simulations gave satisfactory results, a test setup was built. The idea of building first a test setup on a different optical table from the main experiment was to check if the system was working as intended, and assess its performance. Due to physical access problems, in the final system there is no space to place a beam profiler, or a polarimeter, and after the objective there is no access to the vacuum and the trap. While on another table everything could be checked and tested to make sure everything was working as expected. The results of the measurements obtained on this test setup are presented in the next chapter.

Afterwards, the real system was built. The building process was tricky, as the system is particularly sensitive to aberrations. Furthermore, there was not much room for alignment

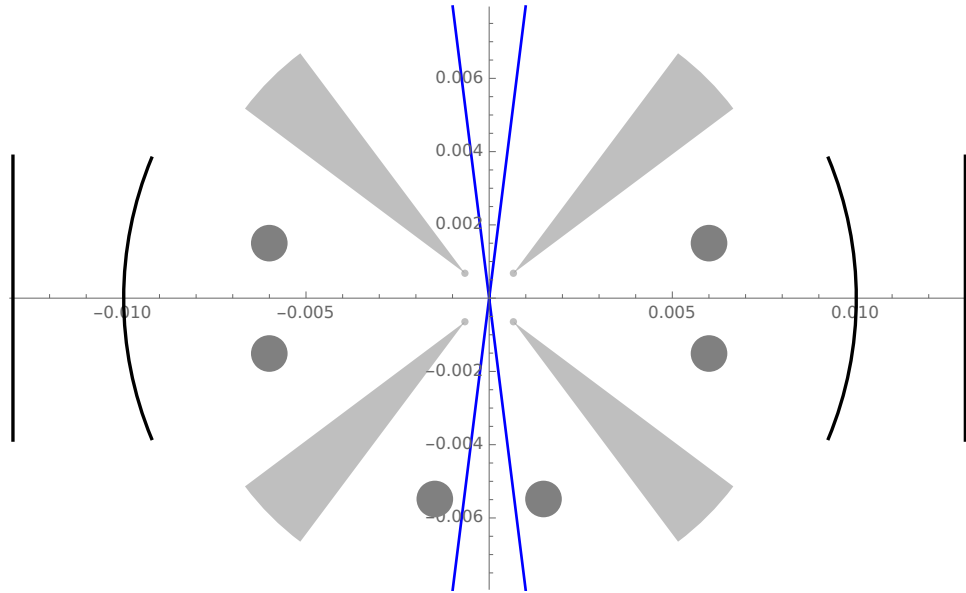


Figure 4.3.6: Top view of the trap and addressing beam. Grey circles are the compensation electrodes, blue is the radius $1/e^2$ of the beam, while the black arches represent the mirrors of the cavity.

errors, since the trap and ion have to be hit perfectly. For this reason the alignment was essential. In order to make sure the addressing beam would hit the ion, a counter propagating red beam was sent in the opposite direction, starting from the ion back to the objective and back to the addressing path. Since the lenses of the addressing are antireflecting coated for 393 nm, the reflection of the red beam was visible and it was possible to align every optical component. For fine tuning calibration, a string of ions was loaded and pulses of 854 nm light were sent at regular interval. The addressed ion was therefore blinking at the set pulse frequency allowing to check the position of the beam on the camera.

The photo of the final system is in figure 4.4.1. Here the collimating lens is mounted on a 3D translation stage with Newport screws for fine tuning calibration of the focus position. Manual screw has been later replaced with remote controlled one always from Newport, model PZA12. An iris is also used to block the zeroth order beam from the AOD. Moreover, The AOD is placed on a rotational mount that allows to tilt it in two directions. One direction was used to find the Bragg angle to achieve maximum diffraction, and the other can be used to tilt the axis over which the AOD sweeps. This can be used to compensate for an ion string which is not exactly parallel to the AOD sweeping direction.



Figure 4.4.1: Photo of the final setup. The blue dashed line is the beam path starting from bottom left at the fiber collimator, all the way to the top where a mirror deflects the beam to send it to the beam splitter.

Chapter 5

Experimental results

This chapter collects all the experimental results obtained during the thesis. Apart from the AOD characterization, there are two main sections. The first one contains the measurements carried out on the test setup done to asses the performance of the system. Here, polarization, stability, and focus spot has been checked. In particular, two methods have been used to measure μm focus spot: razor blade scans, and small pixel size camera. The other section comprises more advanced quantum optic experiments realized with ions and the final installed system. Ramsey spectroscopy was used to check addressing error and focus spot. Moreover, photons have been generated from one single ion with adjacent unperturbed ions.

5.1 AOD

The AOD is the core element of the setup, it is therefore essential to characterize it. The two main parameters we are interested in are the diffraction efficiency and the response time. For the diffraction efficiency we measure the total output power of the light P_{tot} and then the power of the first diffracted order P_1 . Diffraction efficiency is defined as the ratio between the two.

$$\text{DE} = \frac{P_1}{P_{tot}}. \quad (5.1.1)$$

Before measuring the diffraction, the optimal RF power to drive the AOD has been found. This was done by measuring the power at the central frequency of the AOD and maximizing the light in the first diffracted order. Power measurements of the light were done with a Thorlabs PM100D, and the AOD was driven with a signal generator. The optimal RF power was found to be 0.11 W, and for the rest of the measurements it was kept as that value. Furthermore, the input polarization was optimized with a half wave plate, always trying to maximize the power of the diffracted light. In figure 5.1.1 the plot of the diffraction efficiency as a function of the RF frequency is displayed. Within a bandwidth of 50 MHz from 105 MHz to 155 MHz, we can see that more than 70 % of the light is in the first diffracted order as expected from the datasheet, even though the bandwidth looks shifted with respect to the nominal central frequency of 120 MHz. The response time is the time that it takes for the light to move when the RF frequency is changed. In order to perform this measurement, a voltage controlled oscillator (VCO) was used to generate the RF signal. The VCO was supplied a square wave that jumped



Figure 5.1.1: Diffraction efficiency of the AOD as a function of the RF driving frequency.



Figure 5.1.2: Response time of the AOD, plotted are the photodiode signal in blue on the left y axis, and the VCO voltage is in red on the right axis.

between two voltages corresponding to two different frequencies. The blue light was measured with a photodiode. The photodiode was aligned with the light at one particular frequency, such that when the light moves, the beam would not hit the chip and the signal generated changes. In figure 5.1.2, the signal of the photodiode, together with the supplied VCO signal are plotted. Response time is $\sim 7 - 8 \mu\text{s}$, in this time the light completely move from one angle to another one.

5.2 Full test setup characterization

The test setup was built on a spare optical table with a spare objective. The layout of the setup was as close as possible to the final version, so the system in figure 4.1.1 was replicated. The most important assessment was the focus spot, i.e. we tried to measure the waist of the beam and check if it was within requirements. This is measured in two

different ways: first we used a technique called Knife-edge, where the beam is scanned with a razor blade; then we also tried to measure it directly with a camera equipped with $1.6 \mu\text{m}$ pixel size.

Other than the waist size, we also measured stability of the system and the polarization capabilities.

5.2.1 Waist: Knife-Edge method

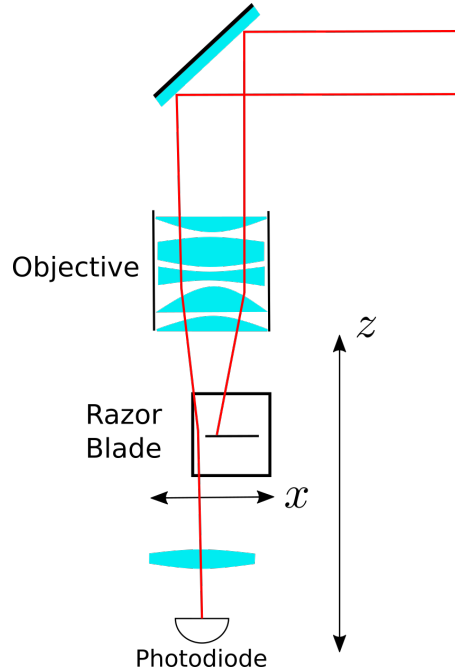


Figure 5.2.1: Scheme of the razor scan. A translation stage allows for moving the blade in two direction x perpendicular to the beam, and z along the beam optical axis.

Measuring a micrometer waist is not easy task, the first approach we tried consists of mounting a razor blade on a translational stage. The stage is then moved in the x direction cutting the beam perpendicularly such that the blade is scanning the beam profile. The setup used is showed in figure 5.2.1, after the objective the blade is present, and since the beam is quickly diverging after the focus, a lens is used to refocus the light into a photodiode. A filter was also inserted in order to not saturate the photodiode. In the z direction the stage was controlled with a manual screw with resolution of $1 \mu\text{m}$. While in the x direction, the stage had to be moved with sub-micrometer precision, so the screw was a piezo actuator controlled by custom software. The same software also controlled a multimeter that measured the voltage of the photodiode. To get the whole profile of the beam, i.e. $W(z)$, the measurement procedure was as follow

- Position blade at appropriate z coordinate
- Scanning beam in x direction with blade
- Beam width extrapolation
- Shift z direction

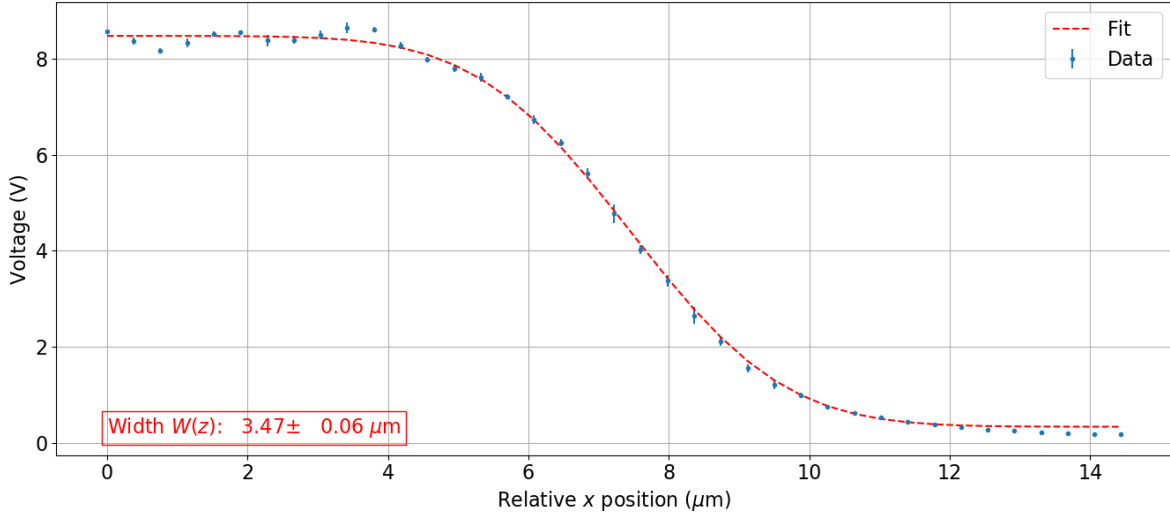


Figure 5.2.2: Example of razor scan

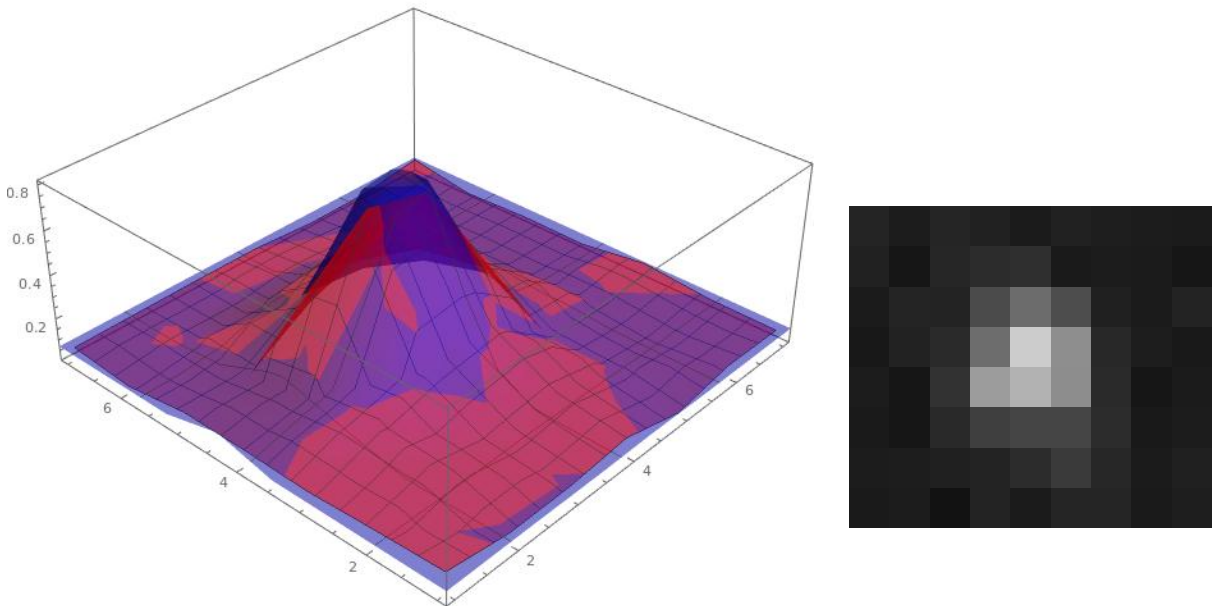
And the procedure is repeated for sufficient values of z to scan at least few Rayleigh ranges. The beam width can be calculated from the scans by fitting the data with [48]

$$P(x, z) = \frac{P_0}{2} \operatorname{erfc} \left[\frac{\sqrt{2}(x - x_0)}{W(z)} \right]. \quad (5.2.1)$$

Where the fitting parameters are P_0 , x_0 , and the width $W(z)$. An example of scan is in figure 5.2.2. The errorbars comes from statistical average, every data point is a mean over 5 measurement, and the error is the standard deviation. The fit in this case gave a width of $3.47 \pm 0.06 \mu\text{m}$, the smallest width obtained with this method. Unfortunately, it is broader than the initial expectations. Furthermore, the profile $W(z)$ did not look symmetric and could not be fitted with equation (2.4.3). A possible explanation is that this method is not suitable for measuring micrometer waists with a razor blade, the roughness of the surface could limit the result. In comparison, authors of [49] have used, instead of a common razor blade, a glass substrate etched with an effective knife-edge feature.

5.2.2 Waist: Camera

Since the Knife-Edge method did not demonstrate particularly effective, if not to give an upper bound to the waist, a more direct approach has been subsequently adopted. We look directly into the beam with a camera from IDS model UI-1490LE-M-GL. This particular camera has a pixel size of $1.6 \mu\text{m}$, with no pixel-pixel distance. It should therefore be suitable to measure a focus spot better than the razor blade. A μm focus should hit one single pixel, and if aligned between two pixels, a Gaussian profile could also be fitted. In addition, unlike the Knife-Edge technique, a camera provides 2-dimensional information about the beam shape and can be exploited to look for aberrations in the system. The setup is almost the same as figure 5.2.1, but the camera now replaces the razor blade, and there is no need for scanning in the x direction, as the z is enough to reconstruct the profile $W(z)$. An additional gradient filter was used to optimize the light reaching the



(a) Fitted data from the camera. In red color, the normalized pixel value is displayed, while the blue curve is a fitted 2D Gaussian. On the axis there is the pixel number

(b) Original photo from the camera.

Figure 5.2.3

camera in order to not saturate it and get a visible signal. The measurement procedure is also similar to the Knife-Edge case. For every desired z displacement, a photo with the camera is taken, post processed, and then the camera is displaced to the new z coordinate. Post processing is done by fitting the pixel values with a 2-dimensional Gaussian

$$P = A \exp \left\{ -\frac{(x - x_0)^2}{2\sigma_x^2} \right\} \exp \left\{ -\frac{(y - y_0)^2}{2\sigma_y^2} \right\}. \quad (5.2.2)$$

The fit parameters are A, x_0, y_0, σ_x , and σ_y . From the standard deviation σ_x and σ_y the width $W(z)$ in the x and y direction can be determined as $W_x = 2 \cdot 1.6 \cdot \sigma_x$ and respectively $W_y = 2 \cdot 1.6 \cdot \sigma_y$, where $1.6 \mu\text{m}$ is the pixel size. In figure 5.2.3, an example of the measurement taken is displayed. The full profiles $W_x(z)$ and $W_y(z)$ can be found in figure 5.2.4. Even here anomalies can be noticed. The profile is asymmetric and does not follow equation 2.4.3, however a width $< 2.5 \mu\text{m}$ has been measured. There could be some reasons behind this result, in some camera pictures some aberrations were visible. Moreover, some estimation error lead to non ideal placement of the lenses. Nonetheless, the smallest measured waist was satisfactory and enough for proceeding with the installation and doing more advanced experiments. But first few more characteristics of the system had to be tested, namely polarization and stability.

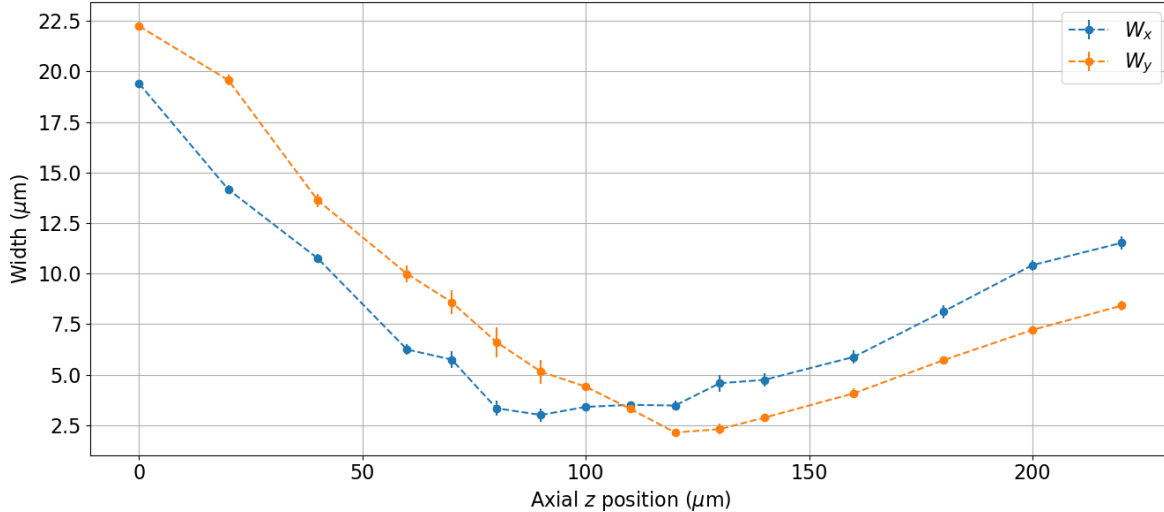


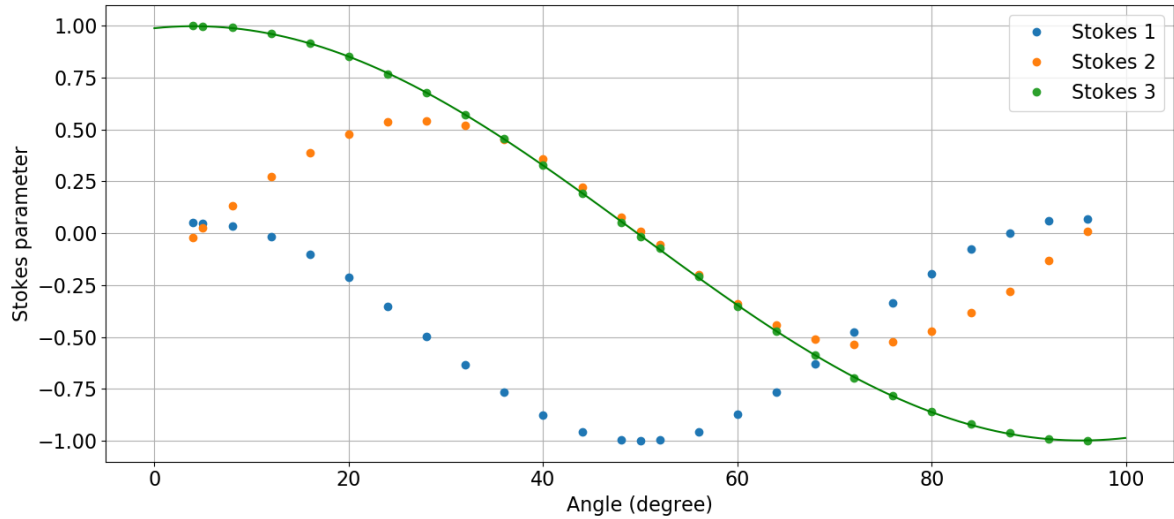
Figure 5.2.4: Profile of the Gaussian beam along z measured with the camera.

5.2.3 Polarization

As discussed in the design section, polarization is an important component of the Raman process, thus the polarization capabilities of the system had to be tested. The goal is to achieve vertical, horizontal, left circular, and right circular polarization at the ion position. Polarization can be changed with two plates: a half wave plate after the AOD, and a quarter wave plate right before the objective, see figure 4.1.1. In order to characterize the polarization, the three Stokes parameters [50] has been measured with a polarimeter from Scäfter + Kirchhoff series SK010PA. Stokes parameters quantify the type of polarization of an electric field. Linear polarized light (vertical and horizontal) has all Stokes parameters set to 0, apart from the first one. Instead, the third parameter, when the others are zero, contains information about circular polarized light which goes from right to left. By rotating a plate and fitting a sine function to the appropriate Stokes parameter, it is possible to gain insights on the appropriate angle to set in order to obtain the desired polarization.

The first step was to characterize the $\lambda/2$ plate alone, the main result from this characterization is that horizontal polarization can be achieved with an angle of $267.2 \pm 0.1^\circ$, and vertical is achieved with an angle of $312.5 \pm 0.1^\circ$ obtained from fitting a sine on the first Stokes parameter. From the same fit, the semiperiod of the polarization is $45.3 \pm 0.6^\circ$. As the mirror can change the polarization, the same characterization has been done after the mirror finding that the polarization is altered unless it is either horizontal or vertical. However the main result was obtained when the $\lambda/4$ was characterized. With every plate inserted, two measurements were made. In the first one the $\lambda/2$ was set to 267° to get horizontal polarization, and the angle of the $\lambda/4$ scanned. This result is presented in figure 5.2.5. The third Stokes parameter is fitted with a sine function to get the angles at which the polarization is right and left circular. The right circular polarization is obtained at the maximum of the curve, while the left corresponds to the minimum. Moreover, when the third Stokes parameter is zero, the polarization results linear. The results are shown in table 5.2.1. The second measurement also scanned the angle of the $\lambda/4$ plate, but this time the $\lambda/2$ was set to 312° such that the polarization before the $\lambda/4$ plate was vertical. In figure 5.2.6 the data is displayed. Again, to get the angle for the different polarizations,

Polarization	$\lambda/2$ ($^{\circ}$)	$\lambda/4$ ($^{\circ}$)
Horizontal	267.2 ± 0.1	49.7 ± 0.1
Vertical	312.5 ± 0.1	48.1 ± 0.1
Right circular	267.2 ± 0.1	4 ± 0.1
Right circular	312.5 ± 0.1	93.1 ± 0.1
Left circular	267.2 ± 0.1	95.4 ± 0.1
Left circular	312.5 ± 0.1	3.1 ± 0.1

Table 5.2.1: Angles**Figure 5.2.5:** Polarization after the objective as a function of the $\lambda/4$ angle with $\lambda/2$ set to horizontal (267°). Green line is a sine function fit.

a sine function was fitted to the third Stokes parameter. The results yielded by the fit are summarized in table 5.2.1.

5.2.4 Stability

In the future the addressing system will be used for long experiments, it is therefore imperative to know the stability of the system in terms of polarization and beam pointing. This means knowing over the course of hours or days if the setup needs to be calibrated. Let us start with polarization stability, the polarization was measured with a polarimeter from Scäfter + Kirchhoff series SK010PA after the objective. The polarization was set to be right circular: $\lambda/2$ set to 267° , and $\lambda/4$ set to 4° . We recorded the three Stokes parameters for a total of one hour, this data is plotted in figure 5.2.7. To the third parameter, 0.998 has been subtracted during the plot such that it would fit with the others. It can be seen that the polarization is stable over a period of one hour.

Beam pointing stability regards the stability of the focus position, which could drift in any direction for any reason. To test the stability, we recorded the position of the focus for a period of one hour with the camera IDS model UI-1490LE-M-GL. The camera was positioned at the focus with the same setup discussed in section 5.2.2, and then a video

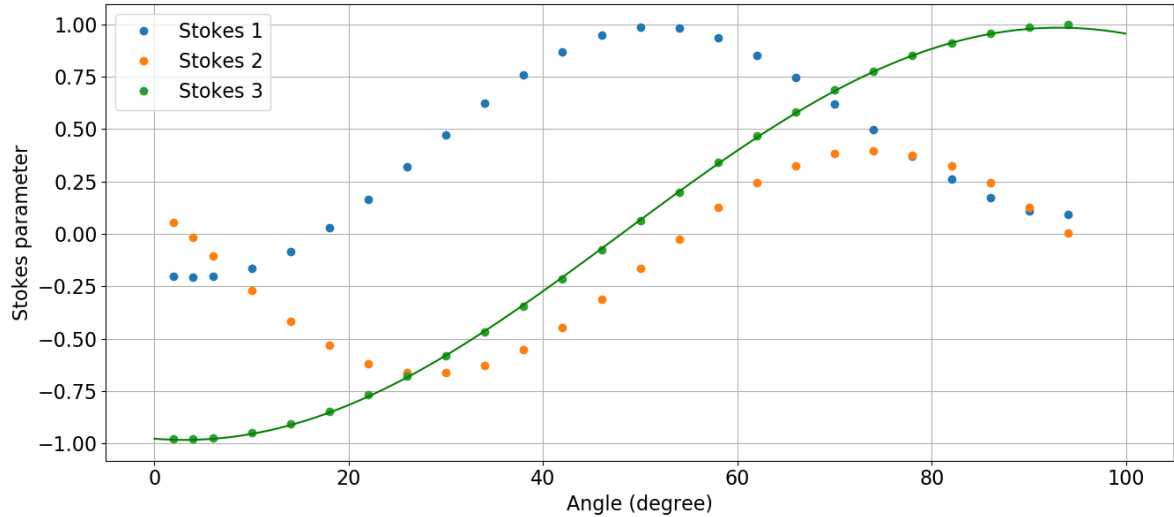


Figure 5.2.6: Polarization after the objective as a function of the $\lambda/4$ angle with $\lambda/2$ set to vertical (314°). Green line is a sine function fit.

was recorded. The video was later analyzed by tracking the the brightest pixel over time. In figure 5.2.8 we can see the horizontal x and vertical y position of such pixel. In the horizontal directions, fluctuations of one single pixel can be noticed, which could be a result of the light hitting between two pixels. In the vertical direction over it looks like the fluctuations are on the order of two pixels, if one consider one pixel a normal fluctuation, then the position might have shifted by one pixel over this period. This means that the focus position is stable with an upperbound of $1.6 \mu\text{m}/\text{hour}$.

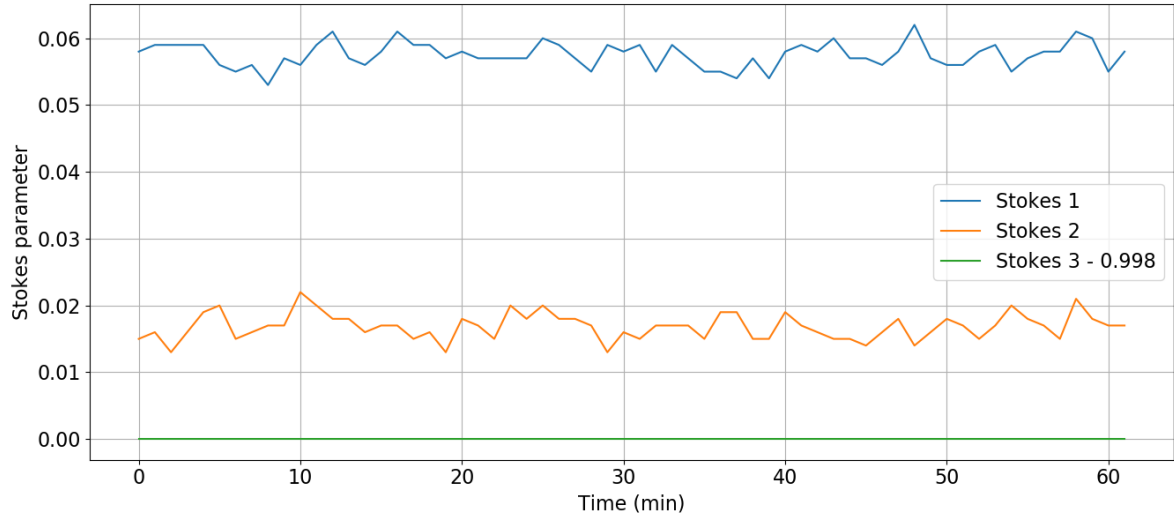


Figure 5.2.7: Right circular polarization stability over a period of one hour.

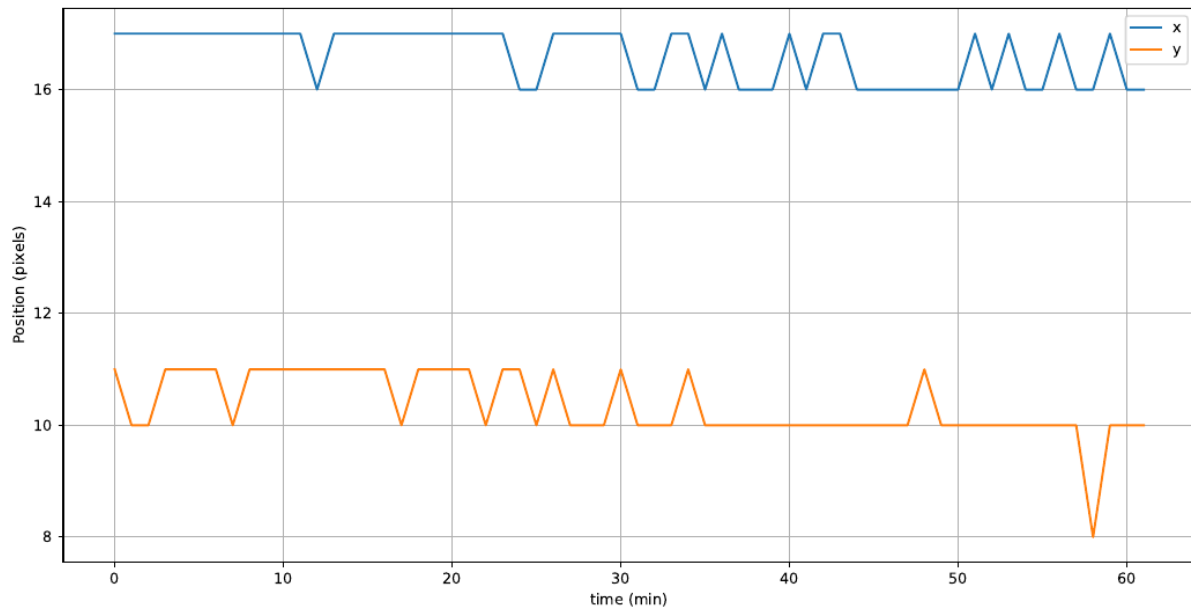


Figure 5.2.8: Beam pointing stability over a period of one hour.

5.3 Final installed system

After the tests presented in the previous sections, the setup was installed next to the ion chamber and focused on the ions as described in section 4.4. As there is no more physical access to the focus spot, more advanced quantum optics experiment have to be carried out in order to measure properties of the system as focus spot and addressing error. The first experiment designed aims exactly at measuring these two quantities: Ramsey fringes were measured on four loaded ions, from which the beam shape can be inferred. The second experiment that we have done involves three ions and the goal was to generate photons via Raman process from one single ion leaving the state of the other two unaltered, demonstrating therefore the possibility to emit single photons from individual ions in a string.

5.3.1 Ramsey interferometry

Once the lasers were all set, four ions were loaded with endcap voltages of 714 V and 700V, and the parameters of the experiment optimized. What has to be found for the experiment is the length of a $\pi/2$ pulse of 729 nm light and the length τ of the 393nm pulse. For the first parameter, Rabi flops were measured and the length of the $\pi/2$ pulse is directly estimated to be 4.2 μ s. These flops are showed in figure 5.3.1

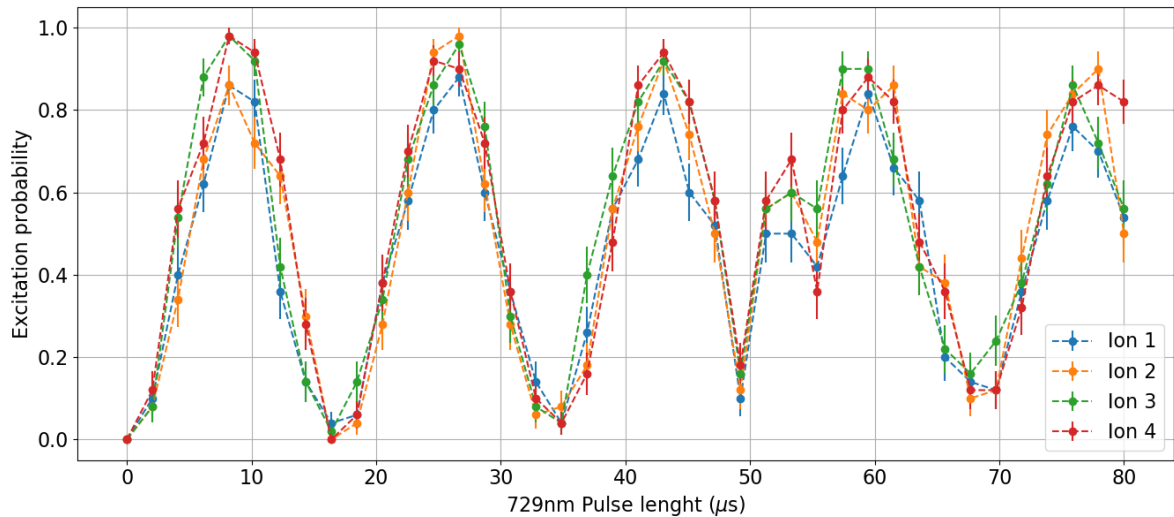


Figure 5.3.1: Rabi flops on 4 ions.

Errorbars on the excitation probability have been assigned according to the error on estimating the probability of a binomial distribution with N number of repetitions.

$$\sigma = \sqrt{\frac{P_D(1 - P_D)}{N}}. \quad (5.3.1)$$

With this value of $\pi/2$ Ramsey fringes were measured, here the ϕ between the two pulses is scanned such that we can decide where to sit for the experiment with the 393nm. The fringes are in figure 5.3.2, as expected the curve follow a $\cos^2(\phi)$ behaviour. In order to

get a better signal, one can decide to sit at the minimum of the curve, i.e. we set for the rest of the experiment $\phi = \pi/2$. The last parameter that has to be decided is the Raman length τ , this value is chosen in a way that the shift caused by the 393nm light does not skip any fringe. This means that if we start from the minimum of figure 5.3.2, the Raman pulse should give an shift that brings the ion at maximum at excitation probability 1, without going further. To get this timing, τ can be scanned and the appropriate value can be visually chosen, the plot is in figure 5.3.4. We set τ to be $25\ \mu\text{s}$, so we climb only about halfway the fringe. Lastly we set the dead time to be $5\ \mu\text{s}$.

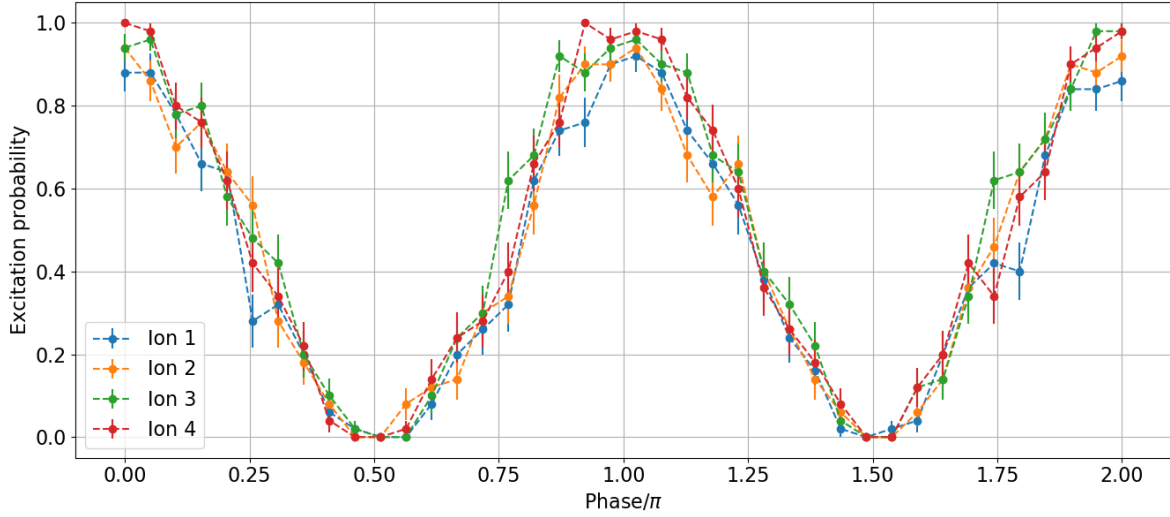


Figure 5.3.2: Ramsey fringes for 4 ions.

To get the profile of the addressing beam, the AOD frequency can be now scanned. During this scan the beam is moved from ion to ion and its shape is probed by the ions. The result after post analysis can be seen in figure 5.3.3. Here the intensity of the beam has been determined from the probability P_D as discussed, errors are propagated accordingly.

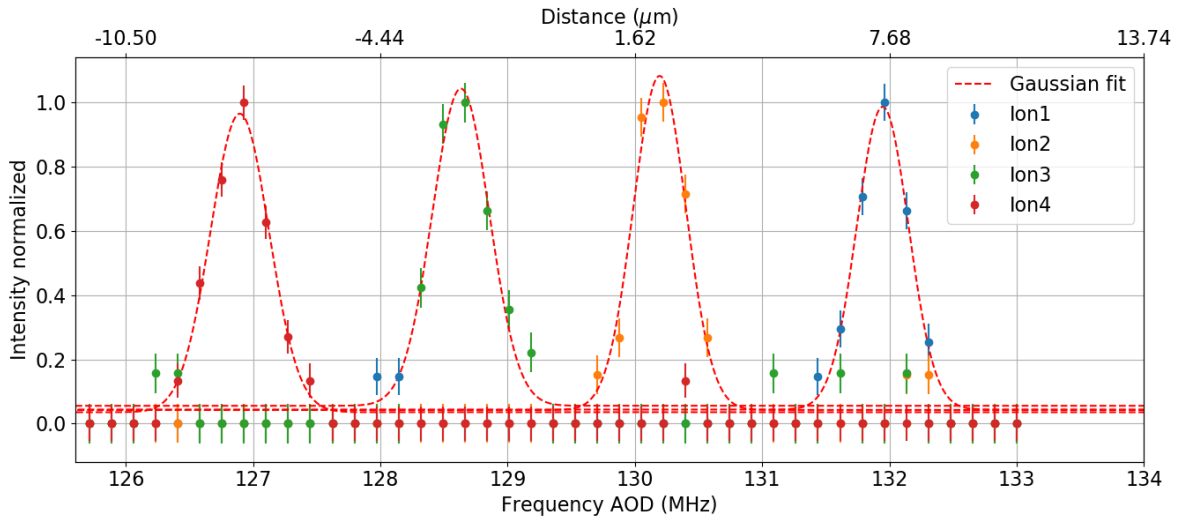


Figure 5.3.3: AOD scanning four ions.

To calibrate the micrometer scale, the position in MHz of two peaks have been taken, then from the axial frequency the position of the ions in the trap can be estimated (cfr. section 2.3.2), by comparing the two values the conversion factor is found.

The four peaks have been fitted with a Gaussian function to obtain the waist of the beam when focused on the different ions. The waist yielded by the fits are from right to left are $\omega_1 = 1.23 \pm 0.20 \mu\text{m}$, $\omega_2 = 1.25 \pm 0.19 \mu\text{m}$, $\omega_3 = 1.35 \pm 0.22 \mu\text{m}$, $\omega_4 = 1.39 \pm 0.20 \mu\text{m}$.

The addressing error can also be estimated from the Stark flops in figure 5.3.4. In this measurement, the addressing beam was focused on one ion and the Raman length τ is scanned. This increases the interaction time of the laser with the ions, and if the interaction is long enough even the tail of a Gaussian can induce some excitation on the ions on the side of the one being addressed. In the scan displayed, the pulse reached $300 \mu\text{s}$ and there is no excitation on any ion apart from the one flopping. Others scans went up to $500 \mu\text{s}$, and still no visual excitation is present. While this means that no quantitative number can be determined for the addressing error, an upper bound can still be given. For an excitation to appear right after $500 \mu\text{s}$, the addressing error should be at most $\Omega_2^2/\Omega_3^2 < 10^{-3}$ (?)

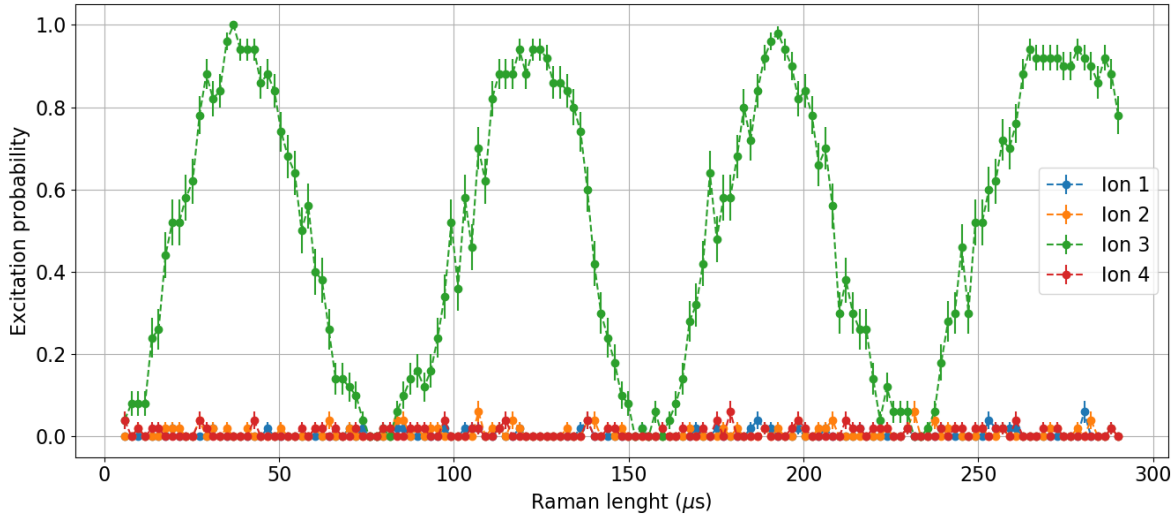


Figure 5.3.4: 393nm AC-Stark flops

5.3.2 Photon production

The main goal of having an addressed 393nm setup is to generate single photon from individual ion in a chain. In this experiment we tested this feature by loading a string of 3 ions, and monitoring the photon generation and the ions state as well. A single photon is produced by a pulse of 393nm light focused on the central ion of three via Raman process. In the experiment we scanned the length of this pulse to obtain an integrated wavepacket, i.e. the cumulative probability of detecting a photon as a function of the pulse length. The generated photon is emitted into the cavity, transmitted through a mirror and couple into a fiber that goes to a superconducting nanowire single-photon detector (SNSPD) which clicks if a photon is detected. The detectors have two channels corresponding to two different photon polarizations. Detuning of the Raman laser is essential in this experiment, so one has to take into account the frequency shift induced by the AOD ~ 127 MHz. As already briefly mentioned, the shift was compensated with the two AOM's in the 393nm

laser setup. The experiment includes an initial stage of Doppler cooling and a final stage of state detection with the PMT. Furthermore, the locking light 806nm in the cavity was switched off during the photon generation process, in this time the cavity maintained its position with a sample and hold. The measurement is repeated N times to get the average photon probability and the excitation probability. These two quantities are plotted in figure 5.3.5 and 5.3.6.

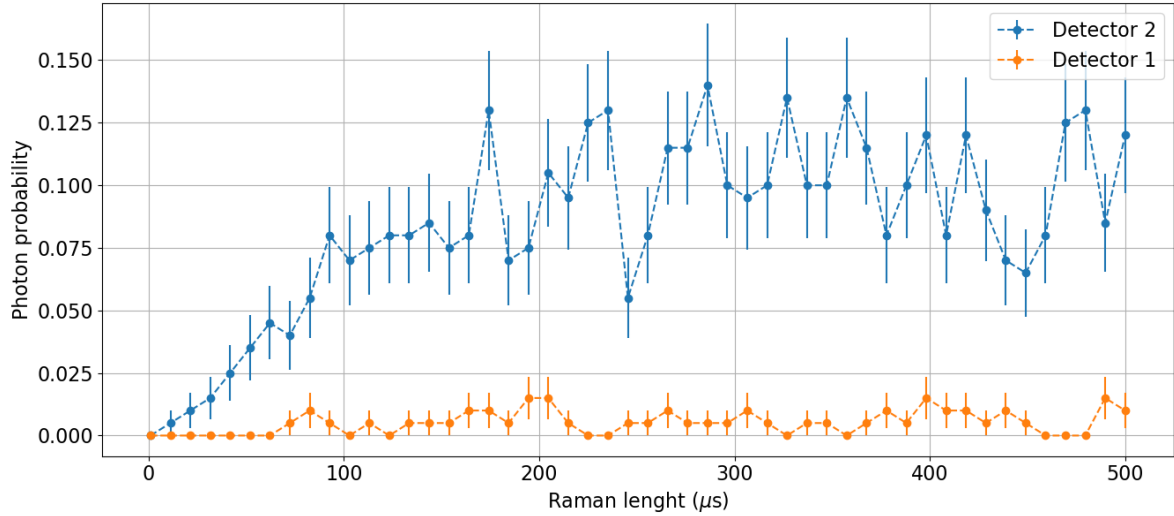


Figure 5.3.5: Integrated photon wavepacket. Cumulative probability of photon generation as a function of the Raman pulse.

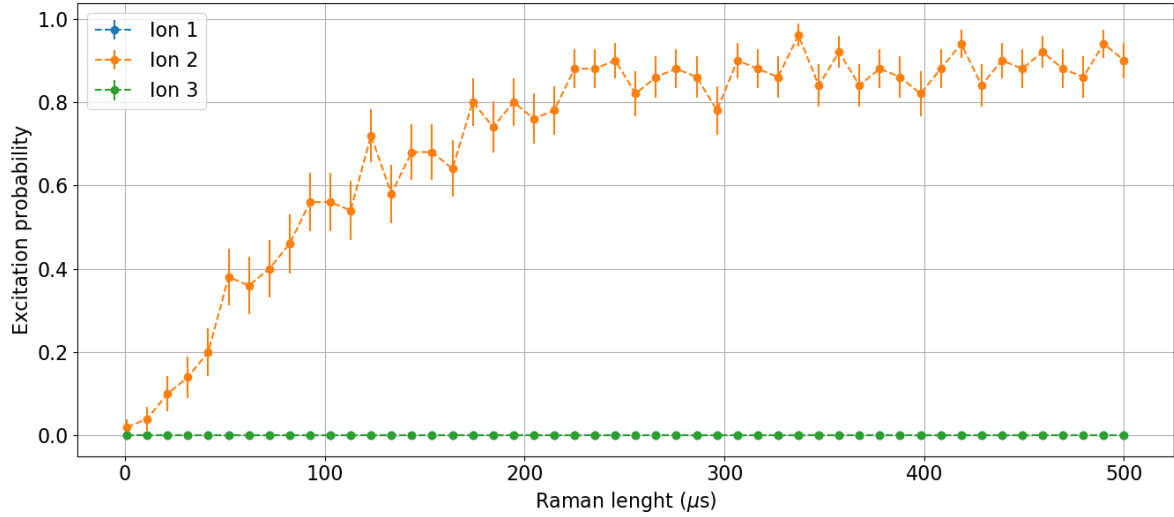


Figure 5.3.6: Qubit state of the ions after sending a Raman pulse.

Errorbars on the excitation probability are calculated as the previous section, while for the photon probability the error is given by Poissonian statistics [51]

$$\sigma_{ph} = \frac{\sqrt{N_{click}}}{N}, \quad (5.3.2)$$

where N_{click} is the number of times a photon has been detected with respect to the total N repetitions. As we can see, only the addressed ion gets excited as emits a photon. The probability of getting photon is relatively low $< 15\%$, as no optimization were performed to increase it.

5.4 Final properties summary

This section contains a summary of the different properties of the setup, everything can be found in the figure below.

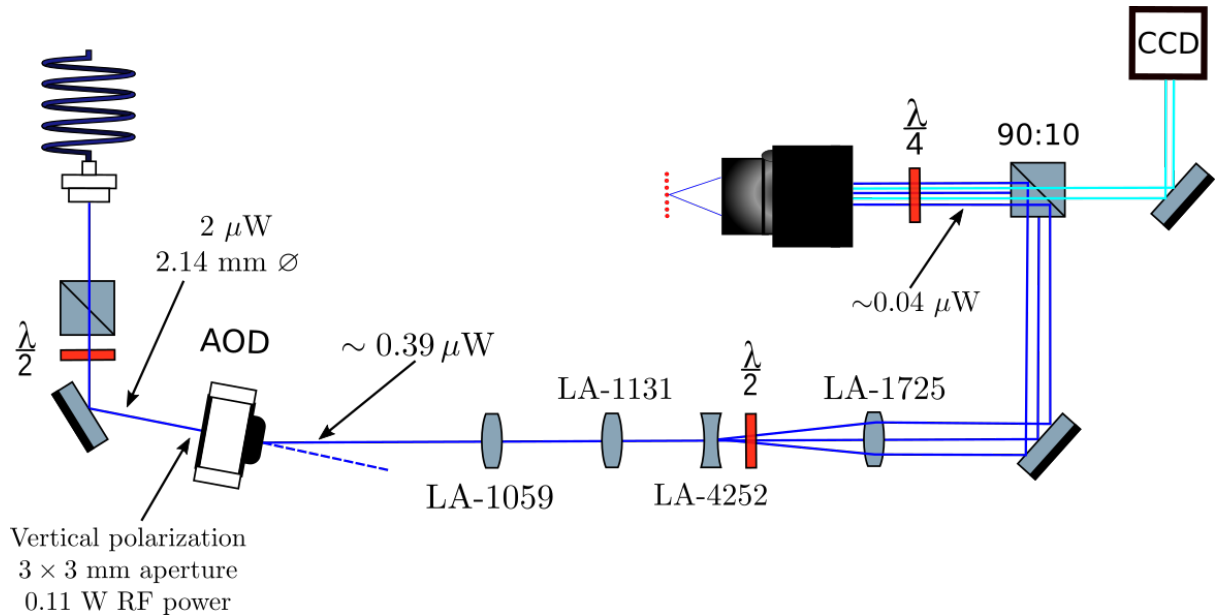


Figure 5.4.1: Properties summary of the setup.

Chapter 6

Conclusions and outlook

In this thesis works, an optical setup for single ion focusing of 393nm laser has been designed and built. The design was based on the already successful addressing setups built in other experiments, but it has been improved to avoid clipping that limited the addressing range. The software Zemax was used to simulate, and check the performance of the design. Optimal lenses for the construction were also found with the software. Once the simulation was satisfactory, a test setup was built on a spare optical table where it has been characterized in terms of performance, polarization capabilities, and stability. Here the smallest waist measured was $2.4 \mu\text{m}$, the switching time with the AOD were in order of $7\text{--}8 \mu\text{s}$, addressing range should be $>150 \mu\text{m}$ and the setup showed to be stable for at least one hour. Afterwards, the setup was moved and aligned with the experiment, where limited physical access did not allow for such easy checks, but instead more advanced quantum optics experiment could have been performed.

The setup was intended to be used for single photon generations and single qubit manipulations. Both of the purposes has been filled: the photon generation was demonstrated in experiment in section 5.3.2, here a string of three ions was loaded into the trap and the focused laser aligned with the central one. A laser pulse triggered the photon generation exclusively from the intended ion as we can see from the excitation probability. The photon detection probability was low $< 15\%$, and can definitely be further improved. Qubit manipulation was carried out in the Ramsey interferometer experiment, here we measured the AC stark shift caused by the 393nm light by imprinting a phase on the qubit encoded in the 729nm transition. State readout of the qubit showed the different final states for different phases. Moreover, with this experiment the waist of beam was measured to be $1.2 - 1.3 \mu\text{m}$ and the addressing error to have an upper bound of 10^{-3} .

The setup can still be optimized, during the experiments, particular attention was not given to the polarization, but the system already has the capabilities for precise polarization setting. Permanent magnets are still mounted parallel to the previous Raman laser direction, they have to be moved in the new direction.

The next natural step is the generation of photons from different ions which requires all ions to be coupled to the cavity vacuum standing wave, a non trivial problem. Entanglement can also be produced between a single ion and a photon, once more stabilization improvement on the setup are done.

This project has several future development, on the quantum network side, this work represents an improved interface between network and quantum computer, transmission

bandwidth has drastically increased, dedicated qubits for networking, storing, and computation can now be created and manipulated. It also opens up to the possibility to create multi-ion-multi-photon states with applications in quantum metrology.

Bibliography

- [1] Antonio Acín, Immanuel Bloch, Harry Buhrman, Tommaso Calarco, Christopher Eichler, Jens Eisert, Daniel Esteve, Nicolas Gisin, Steffen J Glaser, Fedor Jelezko, Stefan Kuhr, Maciej Lewenstein, Max F Riedel, Piet O Schmidt, Rob Thew, Andreas Wallraff, Ian Walmsley, and Frank K Wilhelm. The quantum technologies roadmap: a european community view. *New Journal of Physics*, 20(8):080201, aug 2018.
- [2] Peter W. Shor. Polynomial-time algorithms for prime factorization and discrete logarithms on a quantum computer. *SIAM J. Comput.*, 26(5):1484–1509, oct 1997.
- [3] Lov K. Grover. A fast quantum mechanical algorithm for database search. In *Proceedings of the Twenty-eighth Annual ACM Symposium on Theory of Computing*, STOC ’96, pages 212–219, New York, NY, USA, 1996. ACM.
- [4] Stephanie Wehner, David Elkouss, and Ronald Hanson. Quantum internet: A vision for the road ahead. *Science*, 362(6412), 2018.
- [5] *Proceedings of IEEE International Conference on Computers, Systems and Signal Processing*, 1984.
- [6] Ivan B. Damgård, Serge Fehr, Louis Salvail, and Christian Schaffner. Cryptography in the bounded quantum-storage model. In *Proceedings of the 46th Annual IEEE Symposium on Foundations of Computer Science*, FOCS ’05, pages 449–458, Washington, DC, USA, 2005. IEEE Computer Society.
- [7] Joseph F. Fitzsimons. Private quantum computation: an introduction to blind quantum computing and related protocols. *npj Quantum Information*, 3(1), jun 2017.
- [8] P. Kómár, E. M. Kessler, M. Bishof, L. Jiang, A. S. Sørensen, J. Ye, and M. D. Lukin. A quantum network of clocks. *Nature Physics*, 10(8):582–587, jun 2014.
- [9] Daniel Gottesman, Thomas Jennewein, and Sarah Croke. Longer-baseline telescopes using quantum repeaters. *Phys. Rev. Lett.*, 109:070503, Aug 2012.
- [10] Vasil S. Denchev and Gopal Pandurangan. Distributed quantum computing: A new frontier in distributed systems or science fiction? *SIGACT News*, 39(3):77–95, September 2008.
- [11] David P. DiVincenzo. The physical implementation of quantum computation. *Fortschritte der Physik*, 48(9-11):771–783, 2000.
- [12] Colin D. Bruzewicz, John Chiaverini, Robert McConnell, and Jeremy M. Sage. Trapped-ion quantum computing: Progress and challenges. *Applied Physics Reviews*, 6(2):021314, 2019.

- [13] J. I. Cirac and P. Zoller. Quantum computations with cold trapped ions. *Phys. Rev. Lett.*, 74:4091–4094, May 1995.
- [14] Andreas Stute, Bernardo Casabone, Bernhard Brandstätter, Dr. M. Habicher, H. G. Barros, Piet O. Schmidt, Tracy E. Northup, and Rainer Blatt. Toward an ion–photon quantum interface in an optical cavity. *Applied Physics B*, 107:1145–1157, 2012.
- [15] Isaac L. Chuang Michael A. Nielsen. *Quantum computation and quantum information*. Cambridge Series on Information and the Natural Sciences. Cambridge University Press, 1 edition, 2004.
- [16] H. Häffner, S. Gulde, M. Riebe, G. Lancaster, C. Becher, J. Eschner, F. Schmidt-Kaler, and R. Blatt. Precision measurement and compensation of optical stark shifts for an ion-trap quantum processor. *Phys. Rev. Lett.*, 90:143602, Apr 2003.
- [17] Cornelius Hempel. *Digital quantum simulation, Schroedinger cat state spectroscopy and setting up a linear ion trap*. PhD thesis, University of Innsbruck, 2014.
- [18] Daniel Adam Steck. Quantum and atom optics.
- [19] D.F.V. James. Quantum computation with hot and cold ions: An assessment of proposed schemes. *Fortschritte der Physik*, 48(9-11):823–837, 2000.
- [20] H. J. Kimble. The quantum internet. *Nature*, 453(7198):1023–1030, jun 2008.
- [21] L.-M. Duan and C. Monroe. Colloquium: Quantum networks with trapped ions. *Rev. Mod. Phys.*, 82:1209–1224, Apr 2010.
- [22] Richard J Hughes, Jane E Nordholt, Derek Derkacs, and Charles G Peterson. Practical free-space quantum key distribution over 10 km in daylight and at night. *New Journal of Physics*, 4:43–43, July 2002.
- [23] Stephan Ritter, Christian Nölleke, Carolin Hahn, Andreas Reiserer, Andreas Neuzner, Manuel Uphoff, Martin Mücke, Eden Figueroa, Joerg Bochmann, and Gerhard Rempe. An elementary quantum network of single atoms in optical cavities. *Nature*, 484(7393):195–200, apr 2012.
- [24] W. K. Wootters and W. H. Zurek. A single quantum cannot be cloned. *Nature*, 299(5886):802–803, oct 1982.
- [25] H.-J. Briegel, W. Dür, J. I. Cirac, and P. Zoller. Quantum repeaters: The role of imperfect local operations in quantum communication. *Phys. Rev. Lett.*, 81:5932–5935, Dec 1998.
- [26] Jian-Wei Pan, Christoph Simon, Časlav Brukner, and Anton Zeilinger. Entanglement purification for quantum communication. *Nature*, 410(6832):1067–1070, April 2001.
- [27] L.-M. Duan, M. D. Lukin, J. I. Cirac, and P. Zoller. Long-distance quantum communication with atomic ensembles and linear optics. *Nature*, 414(6862):413–418, nov 2001.
- [28] Charles H. Bennett, Gilles Brassard, Claude Crépeau, Richard Jozsa, Asher Peres, and William K. Wootters. Teleporting an unknown quantum state via dual classical and einstein-podolsky-rosen channels. *Phys. Rev. Lett.*, 70:1895–1899, Mar 1993.

- [29] Helene Hainzer. Laser locking for trapped-ion quantum networks. Master's thesis, University of Innsbruck, 2018.
- [30] Helmut Ritsch, Peter Domokos, Ferdinand Brennecke, and Tilman Esslinger. Cold atoms in cavity-generated dynamical optical potentials. *Rev. Mod. Phys.*, 85:553–601, Apr 2013.
- [31] Philip E. Miller and M. Bonner Denton. The quadrupole mass filter: Basic operating concepts. *Journal of Chemical Education*, 63(7):617, 1986.
- [32] D. Leibfried, R. Blatt, C. Monroe, and D. Wineland. Quantum dynamics of single trapped ions. *Rev. Mod. Phys.*, 75:281–324, Mar 2003.
- [33] D. F. V. James. Quantum dynamics of cold trapped ions with application to quantum computation. *Applied Physics B: Lasers and Optics*, 66(2):pp. 181–90.
- [34] Gabriel Andres Areneda Machuca. *Experiments with single photons emitted by single atoms*. PhD thesis, University of Innsbruck, 2019.
- [35] Bahaa E. A. Saleh and Malvin Carl Teich. *Fundamentals of photonics*. Wiley Series in Pure and Applied Optics, 2 edition, 2007.
- [36] C. S. Williams. Gaussian beam formulas from diffraction theory. *Appl. Opt.*, 12(4):872–876, Apr 1973.
- [37] R. Pieper, D. Koslover, and H. Ndwata. Combining phased array and hamming sound apodization techniques to improve the acousto-optic diffraction bandwidth. In *2009 41st Southeastern Symposium on System Theory*, pages 311–316, March 2009.
- [38] H. Ball, M. W. Lee, S. D. Gensemer, and M. J. Biercuk. A high-power 626 nm diode laser system for beryllium ion trapping. *Review of Scientific Instruments*, 84(6):063107, 2013.
- [39] M. R. Dietrich, N. Kurz, T. Noel, G. Shu, and B. B. Blinov. Hyperfine and optical barium ion qubits. *Phys. Rev. A*, 81:052328, May 2010.
- [40] D. J. Berkeland. Linear paul trap for strontium ions. *Review of Scientific Instruments*, 73(8):2856–2860, 2002.
- [41] H. C. Nägerl, Ch. Roos, D. Leibfried, H. Rohde, G. Thalhammer, J. Eschner, F. Schmidt-Kaler, and R. Blatt. Investigating a qubit candidate: Spectroscopy on the $S_{1/2}$ to $D_{5/2}$ transition of a trapped calcium ion in a linear paul trap. *Phys. Rev. A*, 61:023405, Jan 2000.
- [42] U. Tanaka, I. Morita, and S. Urabe. Selective loading and laser cooling of rare calcium isotope $^{43}\text{Ca}^+$. *Applied Physics B*, 89(2):195–200, Nov 2007.
- [43] Andreas tute. *A light-matter quantum interface: ion-photon entanglement and state mapping*. PhD thesis, University of Innsbruck, 2012.
- [44] H. C. Nägerl, D. Leibfried, H. Rohde, G. Thalhammer, J. Eschner, F. Schmidt-Kaler, and R. Blatt. Laser addressing of individual ions in a linear ion trap. *Phys. Rev. A*, 60:145–148, Jul 1999.

- [45] S. Crain, E. Mount, S. Baek, and J. Kim. Individual addressing of trapped $^{171}\text{yb}^+$ ion qubits using a microelectromechanical systems-based beam steering system. *Applied Physics Letters*, 105(18):181115, 2014.
- [46] M. Johanning, A. Braun, N. Timoney, V. Elman, W. Neuhauser, and Chr. Wunderlich. Individual addressing of trapped ions and coupling of motional and spin states using rf radiation. *Phys. Rev. Lett.*, 102:073004, Feb 2009.
- [47] Fiber Collimators 60FC. <https://www.sukhamburg.com/download/fibercollimators60fc.pdf>.
- [48] Yasuzi Suzuki and Atsushi Tachibana. Measurement of the μm sized radius of gaussian laser beam using the scanning knife-edge. *Applied Optics*, 14(12):2809, December 1975.
- [49] Bruce Cannon, Timothy S. Gardner, and Donald K. Cohen. Measurement of $1-\mu\text{m}$ diam beams. *Appl. Opt.*, 25(17):2981–2983, Sep 1986.
- [50] William H. McMaster. Polarization and the stokes parameters. *American Journal of Physics*, 22(6):351–362, 1954.
- [51] Mark Fox. *Quantum optics: an introduction*. Oxford Master Series in Physics, 6. Oxford University Press, USA, 2006.